

Durham Research Online

Deposited in DRO:

27 May 2021

Version of attached file:

Accepted Version

Peer-review status of attached file:

Peer-reviewed

Citation for published item:

Pozzi, Giacomo and De Paola, Nicola and Nielsen, Stefan and Holdsworth, Robert and Tesei, Telemaco and Thieme, Manuel and Demouchy, Sylvie (2021) 'Coseismic fault lubrication by viscous deformation.', *Nature geoscience*, 14 (6). pp. 437-442.

Further information on publisher's website:

<https://doi.org/10.1038/s41561-021-00747-8>

Publisher's copyright statement:

Additional information:

A read-only copy of the Version of Record can be viewed at the following link, via Springer SharedIt:
<https://rdcu.be/ckK9S>

Use policy

The full-text may be used and/or reproduced, and given to third parties in any format or medium, without prior permission or charge, for personal research or study, educational, or not-for-profit purposes provided that:

- a full bibliographic reference is made to the original source
- a [link](#) is made to the metadata record in DRO
- the full-text is not changed in any way

The full-text must not be sold in any format or medium without the formal permission of the copyright holders.

Please consult the [full DRO policy](#) for further details.

Coseismic fault lubrication by viscous deformation

Giacomo Pozzi^{1*}, Nicola De Paola^{1*}, Stefan B. Nielsen¹, Robert E. Holdsworth¹, Telemaco Tesei²,
Manuel Thieme³ and Sylvie Demouchy³.

¹Department of Earth Sciences, Rock Mechanics Laboratory, University of Durham, Durham, DH1 3LE, UK.

²Department of Geosciences, University of Padova, Via Gradenigo 6, I-35131 Padova, IT.

³Geosciences Montpellier, CNRS & Université de Montpellier, UMR5243, 34095 Montpellier, FR.

*Corresponding Authors: giacomo.pozzi@ingv.it, nicola.de-paola@durham.ac.uk

Despite the hazard posed by earthquakes, we still lack fundamental understanding of the processes that control fault lubrication behind a propagating rupture front and enhance ground acceleration. Laboratory experiments show that fault materials dramatically weaken when sheared at seismic velocities ($> 0.1 \text{ m s}^{-1}$). Several mechanisms, triggered by shear heating, have been proposed to explain the coseismic weakening of faults, but none of these mechanisms can account for experimental and seismological evidence of weakening. Here we show that, in laboratory experiments, weakening correlates to local temperatures attained during seismic slip in simulated faults for diverse rock-forming minerals. The fault strength evolves according to a simple, material-dependent Arrhenius-type law. Microstructures support this observation by showing the development of a principal slip zone with textures typical of sub-solidus viscous flow. We show evidence that viscous deformation (either at sub- or super-solidus temperatures) is an important, widespread and quantifiable coseismic lubrication process. The operation of these highly effective fault lubrication processes means that more energy is then available for rupture propagation and the radiation of hazardous seismic waves.

Earthquakes are amongst the deadliest natural disasters, with statistics showing a global death toll of $> 50,000$ per year, in the period 2000-2016¹. Despite their impact on society, there is still a lack of fundamental understanding about earthquake constitutive behaviour. During seismic events, part of the mechanical energy stored in the stressed rocks is dissipated by frictional heating along the fault, causing the local temperatures to rise^{2,3}. This promotes the onset of thermally-activated weakening mechanisms that help to reduce the shear strength⁴⁻⁶ in the fast sliding portion of the fault, behind the rupture front^{2,3}. Efficient lubrication means that more elastic energy can be transferred to the rupture tip,

31 promoting earthquake propagation and enhancing the dissipation of energy into hazardous seismic
32 waves^{7,8}. Therefore, the characterisation and quantification of weakening mechanisms associated with
33 the faulting process are crucial issues in seismology and fault mechanics⁷.

34 In the last decades, several weakening mechanisms have been proposed on the basis of theoretical
35 models and results of laboratory friction experiments that simulate high-velocity seismic slip in rocks.
36 Among these, the flash heating model^{5,9} is important thanks to its general formulation. However, flash
37 weakening mechanism relates to the concept of load-bearing asperities and does not consider their
38 evolution during slip. With increasing slip, pressures and temperatures, flash heating is likely to evolve
39 to other thermally-controlled processes^{4,5} such as frictional melting^{10–12} (common in silicate rocks) or
40 thermal pressurisation^{13,14} (due to fluids initially present in the fault or released by thermal
41 decomposition processes). Other weakening mechanisms proposed include powder lubrication^{15,16},
42 silica gel lubrication¹⁷ and thermal decomposition¹⁸. More recently, an alternative weakening
43 mechanism has been described in experiments using carbonate gouges, where coseismic deformation
44 is accommodated by ductile creep mechanisms^{19–22}. Despite this wide range of weakening mechanisms
45 described in literature, the processes involved in fault lubrication are still not fully understood. In
46 particular, there is no quantitative model for fault lubrication during earthquake slip⁴ in fine-grained
47 granular material (i.e., fault gouges) that can account for both experimental and seismological
48 observations, and also be fully supported by microstructural studies (melt lubrication aside^{10,12,23}).

49 Here we investigate coseismic weakening mechanisms in several rock-forming minerals by integrating
50 mechanical data from shear experiments on powders at high velocity ($v > 0.1 \text{ ms}^{-1}$) with microstructural
51 analyses. The results, summarised below, show that the strengths of the analysed materials follow a
52 common temperature-dependent law and develop microstructures consistent with viscous deformation
53 mechanisms.

54 **Shear experiments at seismic velocity**

55 We shear powders (grain size 63–90 μm) of a range of silicate and non-silicate, anhydrous rock-
56 forming minerals (experimental procedure as in Pozzi *et al.*, 2019²², and references therein^{20,21}).
57 Specifically, we tested carbonate (calcite²⁰ and dolomite^{24,25}), sulphate (anhydrite²⁶), halide (halite²⁷)
58 and silicate (olivine^{28,29}) powders, which are commonly used as analogues for a range of natural fault
59 gouges³⁰. These minerals do not produce frictional melts (apart from halite) and do not contain

60 structural water, hydroxyl or hydrogen. The testing materials and conditions were chosen to diminish
61 the efficiency of flash heating processes^{5,31} (by using fine-grained powders) and to exclude the
62 contribution of fluid-driven mechanisms to fault weakening^{10,16,20,21,25}.

63 A normal stress of $\sigma_n = 25$ MPa (20 MPa for olivine) was applied to the gouges, and held constant
64 throughout the tests. The samples were then sheared at room temperature and humidity at different
65 seismic velocities (0.28 to 1.4 m s⁻¹) for ~ 1 m of total slip. This amount of slip is enough to produce
66 weakening, but still not large enough to produce significant thermal decomposition, frictional melting
67 and other physical changes in the rocks^{20,25}.

68 For each experiment, the effective friction coefficient μ^* (i.e., the measured ratio between shear and
69 normal stress, which is not dependent on any particular deformation mechanism) follows a classic
70 weakening profile²¹ (Figure 1a). Initial slip hardening in the Byerlee's range (Stage I; $\mu^* = 0.6 - 0.9$) –
71 almost absent in halite – is followed by an abrupt decay of fault strength to low friction values (Stage II;
72 $\mu^* < 0.4$). Friction then remains low during shearing at constant velocity, showing a slow decay with slip
73 (Stage III in Figure 1a). Partial re-strengthening is observed during the final deceleration and arrest of
74 slip (Stage IV). The bulk temperature in the principal slip zone (PSZ) cannot be measured directly, and is
75 obtained using an equation for one-dimensional thermal diffusion¹³ (Figure 1b, see Methods).

76 **Microstructures and deformation mechanisms**

77 After each run, samples were carefully recovered and cross-sections of the most deformed parts were
78 prepared for microstructural analysis (Figure 2f; Supplementary Figures S3-S11). In all experiments, we
79 observe a principal slip zone (PSZ) with finite thickness of a few tens of microns (Figure 2) that shows
80 marked textural differences with the surrounding materials. The PSZs are characterised by fine-grained
81 polygonal aggregates with extremely low porosity, fairly homogeneous grain size, and oblique foliation²¹
82 (Figure 2). No significant overprint of microstructures is expected in our experiments due to late- and/or
83 post-deformation annealing (Supplementary Section II) nor by local embrittlement during stage IV²¹
84 (white arrows in Figure 2a-e).

85 At high magnifications, within the PSZs, grains show low aspect ratio²² (on an average, nearly equant),
86 display diamond-shapes, quadruple junctions, narrow gaps and numerous grain boundaries aligned with
87 the shear direction (Supplementary Figure S12a-d and Supplementary Section III). These textures are
88 compatible with mechanisms of neighbour-switching that are typical of grain boundary sliding^{32,33} (GBS,
89 Figure 3e). Microstructural analysis in calcite experiments suggests diffusion-accommodated GBS^{19,20,22},

90 although we do not exclude dislocation-accommodated GBS for the other materials. Transmission
91 electron microscope (TEM) imaging in both calcite and olivine shows that PSZ grains contain dislocations
92 (Figure 3f-i), dislocation walls and subgrains (regions bounded by dislocation walls, Figure 3f, i),
93 indicative of dislocation creep (DC) mechanisms. Notably, oblique foliation (Figure 2) development is
94 compatible with both GBS and DC mechanisms^{34,35}.

95 These observations extend recent results of high-velocity experiments in calcite gouges showing that
96 deformation during Stage III slip is controlled by a combination of grain size-sensitive (GBS) and grain
97 size-insensitive (DC) creep mechanisms^{19–22}. Dislocation creep limits the grain growth in the PSZ^{36–38} (i.e.,
98 by formation of subgrains, see Figure 3f), while diffusion-assisted GBS could be instrumental in
99 explaining the measured low stress^{19–22,38}. Microstructural observations from all other materials tested
100 here also support the hypothesis that coseismic deformation is accommodated by viscous processes at
101 sub-melting temperatures.

102 **Arrhenius-type flow law describes coseismic fault strength**

103 Microstructural analyses suggest that the PSZ accommodates almost all of the shear deformation,
104 and maintains constant thickness throughout Stage III²¹, meaning that its strain rate is nearly constant.
105 During Stage III, for each material, the natural logarithm of shear stress vs. the inverse values of
106 calculated temperature (Figure 4a) shows — to a good approximation — a linear trend with specific
107 slope (thick lines in Figure 4b).

108 Exponential regression allows computation of the dependence of fault strength τ on temperature T
109 during Stage III, which follows the equation

$$110 \quad \ln \tau = A \frac{1}{T} + B \quad (1)$$

111 where A and B are best-fit constants. The specific best-fit equations of each material-dependent curve
112 are reported in Figure 4.

114 Ductile creep mechanisms share a similar exponential relationship following the general Arrhenius-type
115 constitutive equation³⁹

$$116 \quad \dot{\gamma} = C^* \frac{\tau^n}{D^m} e^{-\frac{Q}{RT}} \quad (2)$$

117

118 where $\dot{\gamma}$ is the shear strain rate, C^* a pre-exponential constant, D the mean grain size, n and m the stress
119 and grain size exponents, respectively, Q the activation energy and R the gas constant. Eq. 2 can be
120 rearranged⁴⁰ to:

$$\ln \tau = \left[\frac{Q}{nR} \right] \frac{1}{T} + \left[\frac{1}{n} \ln \left(\dot{\gamma} \frac{D^m}{C^*} \right) \right] \quad (3)$$

123 which is directly comparable to Eq. 1.

124 The PSZ grains were simultaneously affected by GBS (Figure 3a) and DC mechanisms (Figure 3c). Our
125 observations confirm the hypotheses formulated by Ashby and Verrall³² in their pioneering work on the
126 flow of superplastic alloys, which predicted that GBS and DC are likely to occur simultaneously in nature.
127 The slope A in Eq. 1 is primarily controlled by the ratio of activation energy Q and stress exponent n ,
128 normalized by the gas constant R (Eq. 3); hence it is not the expression of a single deformation
129 mechanism.

130 The combination of mechanical data and microstructural observations suggests that the flow rate in
131 the PSZ is dominated by the most effective mechanism, which in calcite is arguably some type of
132 diffusion-accommodated GBS^{19–22}. DC is the mechanism that limits the grain growth in the PSZ^{36–38} of
133 calcite samples (e.g., by subgrain rotation²²), and it might become the dominant deformation
134 mechanism in other materials.

135 It is worth noting that the ratio $A = Q/nR$ obtained for all tested materials is significantly lower than
136 that obtained from previous studies performed at lower strain, sub-seismic strain rate and coarser grain
137 size, for both grain size-sensitive and -insensitive creep (Supplementary Section VI). Such previous
138 studies accept that best-fit parameters of flow laws evolve with increasing strain and can be considered
139 constant only for limited ranges of strain^{36–38,41–43}. Looking forwards, our results highlight the need of
140 further research to improve our understanding of the physics of deformation processes across the
141 transition from low to high strain and from sub-seismic to seismic strain rates.

142 The comparison between Eq. 1 and Eq. 3 shows that the intercept B is primarily controlled by strain
143 rate, grain size, grain size exponent m and pre-exponential factor C^* .

144 The linear fit of experimental data and microstructural observations point to a grain size-dependent
145 rheology in which fault strength is mainly controlled by temperature according to an Arrhenius type law,
146 while the interplay of different creep mechanisms adjusts to the evolving conditions.

147 During Stage III, olivine aggregates show a change of dependence of fault stress to temperature
148 (change of slope, A term in Eq. 1) at values above $T \sim 900$ °C (Figure 4b). Such a temperature threshold

corresponds to a homologous temperature (T/T_m) of ~ 0.57 , where the melting temperature of forsterite olivine (Fo90) is $T_m = 1765\text{ }^\circ\text{C}^{28}$. This might suggest a change of the involved deformation mechanisms and reduced material strength, which is consistent with previous studies reporting faster rheological weakening in olivine⁴⁴ when $T > 0.6 T_m$.

Implications for coseismic weakening mechanisms

We have shown that coseismic weakening observed in a range of different minerals is plausibly achieved through viscous deformation along faults. We therefore propose that localisation of deformation into thin PSZs and the associated weakening are likely controlled by a balance between heat production (by shear heating) and dissipation (by thermal diffusion and endothermic processes)^{4,23,45}. The PSZ system will evolve toward its steady-state by the minimization of viscous strain energy, when a stable temperature profile is established across the slip zone at larger amounts of slip⁴. This rheological evolution is similar to that known for coseismic frictional melts where the molten layer properties are controlled by the heat balance across the fault²³. Notably, the melt viscosity that controls the shear resistance of the fault (i.e., friction) is also controlled by a well-constrained Arrhenius-type dependency to temperature^{23,46}. For comparison, see the linear slope in the inset of Figure 4b, which was measured during weakening by melt lubrication of high velocity shear experiments of gabbro²³.

We also note that, in the alternative model of flash heating^{5,13}, bulk weakening is achieved through the temperature rise at the asperity scale, which causes plastic softening and/or melting of contacts^{5,12}. The mechanisms of flash heating are thus likely to also be viscous in nature and not mutually exclusive with our findings. The bulk behaviour of the fault is a function of the distribution and dimensions of asperities, which influence the local energy budget. In conclusion, the difference between flash heating and viscous deformation in a PSZ might simply be related to the scale of observation.

The similarity of the processes involved during coseismic slip is in good agreement with the observed ubiquity of weakening documented at seismic velocities across a wide range of fault materials⁴. Therefore, we propose that coseismic weakening by viscous processes at either sub- (coseismic ultramylonites²²) or super-solidus (frictional melt^{10,12,23}) temperatures is more widespread than previously thought. These mechanisms obey a simple Arrhenius-type dependency to temperature whose thermodynamic parameters can be potentially determined through experimental investigation. Our results offer an alternative, quantitative viewpoint of fault strength-controlling processes, and provide a new perspective on the role of ductile processes active along faults at seismic strain rates.

References

1. Deaths due to earthquakes worldwide. Available at:
<https://www.statista.com/statistics/263108/global-death-toll-due-to-earthquakes-since-2000/>.
2. Kanamori, H. & Rivera, L. Energy partitioning during an earthquake. in *Geophysical Monograph Series* **170**, 3–13 (2006).
3. Nielsen, S. *et al.* G: Fracture energy, friction and dissipation in earthquakes. *J. Seismol.* **20**, 1187–1205 (2016).
4. Di Toro, G. *et al.* Fault lubrication during earthquakes. *Nature* **471**, 494–499 (2011).
5. Goldsby, D. L. & Tullis, T. E. Flash heating leads to low frictional strength of crustal rocks at earthquake slip rates. *Science (80-.)*. **334**, 216–218 (2011).
6. Hirose, T. & Shimamoto, T. Growth of molten zone as a mechanism of slip weakening of simulated faults in gabbro during frictional melting. *J. Geophys. Res.* **110**, B05202 (2005).
7. Scholz, C. H. (Christopher H. . *The Mechanics of Earthquakes and Faulting*. (Cambridge University Press, 2002).
8. Noda, H. & Lapusta, N. Stable creeping fault segments can become destructive as a result of dynamic weakening. *Nature* **493**, 518–521 (2013).
9. Rice, J. R. Flash heating at asperity contacts and rate-dependent friction. *Eos Trans. AGU* **80(46)**, **Fa**, F6811 (1999).
10. Di Toro, G., Hirose, T., Nielsen, S., Pennacchioni, G. & Shimamoto, T. Natural and experimental evidence of melt lubrication of faults during earthquakes. *Science (80-.)*. **311**, 647–649 (2006).
11. Spray, J. G. Frictional Melting Processes in Planetary Materials: From Hypervelocity Impact to Earthquakes. *Annu. Rev. Earth Planet. Sci.* **38**, 221–254 (2010).
12. Hayward, K. S., Hawkins, R., Cox, S. F. & Le Losq, C. Rheological Controls on Asperity Weakening During Earthquake Slip. *J. Geophys. Res. Solid Earth* **124**, 12736–12762 (2019).
13. Rice, J. R. Heating and weakening of faults during earthquake slip. *J. Geophys. Res. Solid Earth* **111**, B05311 (2006).
14. Viesca, R. C. & Garagash, D. I. Ubiquitous weakening of faults due to thermal pressurization. *Nat. Geosci.* **8**, 875–879 (2015).
15. Reches, Z. & Lockner, D. A. Fault weakening and earthquake instability by powder lubrication. *Nature* **467**, 452–455 (2010).

- 209 16. Han, R., Hirose, T. & Shimamoto, T. Strong velocity weakening and powder lubrication of
210 simulated carbonate faults at seismic slip rates. *J. Geophys. Res. Solid Earth* **115**, B03412 (2010).
- 211 17. Di Toro, G., Goldsby, D. L. & Tullis, T. E. Friction falls towards zero in quartz rock as slip velocity
212 approaches seismic rates. *Nature* **427**, 436–439 (2004).
- 213 18. Sulem, J. & Famin, V. Thermal decomposition of carbonates in fault zones: Slip-weakening and
214 temperature-limiting effects. *J. Geophys. Res.* **114**, B03309 (2009).
- 215 19. Green, H. W., Shi, F., Bozhilov, K., Xia, G. & Reches, Z. Phase transformation and nanometric flow
216 cause extreme weakening during fault slip. *Nat. Geosci.* **8**, 448–489 (2015).
- 217 20. De Paola, N., Holdsworth, R. E., Viti, C., Collettini, C. & Bullock, R. Can grain size sensitive flow
218 lubricate faults during the initial stages of earthquake propagation? *Earth Planet. Sci. Lett.* **431**,
219 48–58 (2015).
- 220 21. Pozzi, G., De Paola, N., Nielsen, S. B., Holdsworth, R. E. & Bowen, L. A new interpretation for the
221 nature and significance of mirror-like surfaces in experimental carbonate-hosted seismic faults.
222 *Geology* **46**, 583–586 (2018).
- 223 22. Pozzi, G. *et al.* Coseismic ultramylonites: An investigation of nanoscale viscous flow and fault
224 weakening during seismic slip. *Earth Planet. Sci. Lett.* **516**, 164–175 (2019).
- 225 23. Nielsen, S., Di Toro, G., Hirose, T. & Shimamoto, T. Frictional melt and seismic slip. *J. Geophys.*
226 *Res. Solid Earth* **113**, B01308 (2008).
- 227 24. De Paola, N. *et al.* Fault lubrication and earthquake propagation in thermally unstable rocks.
228 *Geology* **39**, 35–38 (2011).
- 229 25. De Paola, N. *et al.* The geochemical signature caused by earthquake propagation in carbonate-
230 hosted faults. *Earth Planet. Sci. Lett.* **310**, 225–232 (2011).
- 231 26. De Paola, N., Faulkner, D. R. & Collettini, C. Brittle versus ductile deformation as the main
232 control on the transport properties of low-porosity anhydrite rocks. *J. Geophys. Res.* **114**,
233 B06211 (2009).
- 234 27. Buijze, L., Niemeijer, A. R., Han, R., Shimamoto, T. & Spiers, C. J. Friction properties and
235 deformation mechanisms of halite(-mica) gouges from low to high sliding velocities. *Earth*
236 *Planet. Sci. Lett.* **458**, 107–119 (2017).
- 237 28. Thieme, M., Demouchy, S., Mainprice, D., Barou, F. & Cordier, P. Stress evolution and associated
238 microstructure during transient creep of olivine at 1000–1200 °C. *Phys. Earth Planet. Inter.* **278**,
239 34–46 (2018).

- 240 29. Gasc, J., Demouchy, S., Barou, F., Koizumi, S. & Cordier, P. Creep mechanisms in the lithospheric
241 mantle inferred from deformation of iron-free forsterite aggregates at 900–1200 °C.
242 *Tectonophysics* **761**, 16–30 (2019).
- 243 30. Sibson, R. H. Fault rocks and fault mechanisms. *J. Geol. Soc. London.* **133**, 191–213 (1977).
- 244 31. Brantut, N. & Platt, J. D. Dynamic weakening and the depth dependence of earthquake faulting.
245 in *Fault Zone Dynamic Processes: Evolution of Fault Properties During Seismic Rupture* 171–194
246 (2017). doi:10.1002/9781119156895.ch9
- 247 32. Ashby, M. F. & Verrall, R. A. Diffusion-accommodated flow and superplasticity. *Acta Metall.* **21**,
248 149–163 (1973).
- 249 33. Dygert, N., Bernard, R. E. & Behr, W. M. Great Basin Mantle Xenoliths Record Active Lithospheric
250 Downwelling Beneath Central Nevada. *Geochemistry, Geophys. Geosystems* **20**, 751–772 (2019).
- 251 34. Wheeler, J. Anisotropic rheology during grain boundary diffusion creep and its relation to grain
252 rotation, grain boundary sliding and superplasticity. *Philos. Mag.* **90**, 2841–2864 (2010).
- 253 35. Miyazaki, T., Sueyoshi, K. & Hiraga, T. Olivine crystals align during diffusion creep of Earth’s
254 upper mantle. *Nature* **502**, 321–326 (2013).
- 255 36. Poirier, J.-P. *Creep of crystals. . High-temperature deformation processes in metals, ceramics and*
256 *minerals* (Cambridge University Press, 1985). doi:10.1007/978-0-387-09751-0_26
- 257 37. Barnhoorn, A., Bystricky, M., Burlini, L. & Kunze, K. The role of recrystallisation on the
258 deformation behaviour of calcite rocks: Large strain torsion experiments on Carrara marble. *J.*
259 *Struct. Geol.* **26**, 885–903 (2004).
- 260 38. De Bresser, J. H. P., Ter Heege, J. H. & Spiers, C. J. Grain size reduction by dynamic
261 recrystallization: Can it result in major rheological weakening? *Int. J. Earth Sci.* **90**, 28–45 (2001).
- 262 39. Kohlstedt, D. L. Properties of Rocks and Minerals – Constitutive Equations , Rheological Behavior
263 , and Viscosity of Rocks. *Treatise Geophys.* **2**, 389–417 (2007).
- 264 40. Mackwell, S. J. & Paterson, M. S. New developments in deformation studies: High-strain
265 deformation. *Reviews in Mineralogy and Geochemistry* **51**, 1–19 (2002).
- 266 41. Frost, H. J. & Ashby, M. F. *Deformation-mechanism maps: the plasticity and creep of metals and*
267 *ceramics*. (Pergamon Press, 1982).
- 268 42. Schmid, S. M., Boland, J. N. & Paterson, M. S. Superplastic flow in finegrained limestone.
269 *Tectonophysics* **43**, 257–291 (1977).
- 270 43. Pieri, M., Burlini, L., Kunze, K., Stretton, I. & Olgaard, D. L. Rheological and microstructural

evolution of Carrara marble with high shear strain: Results from high temperature torsion experiments. *J. Struct. Geol.* **23**, 1393–1413 (2001).

44. Wang, Q. Homologous temperature of olivine: Implications for creep of the upper mantle and fabric transitions in olivine. *Sci. China Earth Sci.* **59**, 1138–1156 (2016).

45. Handy, M. R. The energetics of steady state heterogeneous shear in mylonitic rock. *Mater. Sci. Eng. A* **175**, 261–272 (1994).

46. Philpotts, A. R. (Anthony R. & Ague, J. J. *Principles of igneous and metamorphic petrology*. (Cambridge University Press, 2009).

Corresponding author details: Correspondence about the manuscript and requests for materials should be addressed to Nicola De Paola (nicola.de-paola@durham.ac.uk) and Giacomo Pozzi (giacomo.pozzi@ingv.it).

Acknowledgments

We thank S. Cox for constructive reviews that helped improve the presentation of the dataset and clarity of the text. We also thank B. Mendis, L. Bowen and F. Barou for their assistance with the acquisition of SEM and TEM images and discussion, and Prof. A. Beeby for acquiring Raman spectra on our samples. This project has received funding from the European Union’s Horizon 2020 research and innovation program under the Marie Skłodowska-Curie grant agreement No 642029 - ITN CREEP to N.D.P, and the Natural Environment Research Council (NERC) through a NERC standard grant NE/H021744/1 to N.D.P.

Author Contributions Statement

G.P. ran the experiments and carried out the microstructural analysis and interpretations. G.P., N.D.P., S.N., R.E.H. and T.T. contributed equally to the concept development and to the writing of the paper. All Authors jointly supervised this work.

Competing Interests Statement

The authors declare no competing interests.

Figure Legends

327 **Figure 1 | Mechanical data.** a) Effective friction coefficient (μ^*) evolving with displacement during
328 Stages I - IV (see text for details). During Stage III, μ^* values are lower in experiments run at higher
329 velocities. Each experiment terminates with partial re-strengthening during deceleration to arrest.
330 b) Shear stress as a function of calculated temperature (up to Stage III). Note that the Stage III
331 mechanical data of calcite, dolomite and anhydrite - and with good approximation for halite and
332 olivine - collapse onto a single material-characteristic curve. Halite curves overlap up to a
333 temperature of $\sim 440^\circ\text{C}$.

334 **Figure 2 | Microstructures.** Fore-scattered (**a,e**) and back-scattered (**b-d**) scanning electron
335 microscope (SEM) images of sample principal slip zones (PSZ) in polished cross sections cut parallel
336 to the slip direction. PSZs are composed by polygonal aggregates with low porosity and fairly
337 homogenous grainsize (close ups in Figure 3). In **a**, **b** and **d** an oblique (white angle) ultramylonitic
338 foliation is visible. White arrows highlight local brittle overprint of Stage IV^{21,22}. **F** shows a
339 schematic cross section of the samples. The rectangle shows the location of the microstructures
340 in panels **a-e**. Inset of panel **f** shows the approximate location of the cross-section (CS) with respect
341 to the whole sheared gouge sample (G). The round arrow shows the shear direction.

342 **Figure 3 | Deformation mechanisms.** **a-d**, SEM images of the grains within the PSZs. The textures
343 were captured using fore-scattered electron (**a**) back-scattered electron (**b**, **c**) and EBSD band
344 contrast (**d**) imaging. Sense of shear is top-to-the-left. Polygonal grains show fairly equant to
345 slightly elongated shapes. Grains are diamond-shaped and commonly display: quadruple junctions
346 (sets of four grains highlighted in green and yellow); boundaries aligned with the shear direction;
347 and narrow gaps. Neighbour-switching processes typical of grain boundary sliding³² are sketched
348 in **e**, where grains are coloured in green and yellow for comparison with **a-d**. (**f-i**) Transmission
349 electron images of the PSZ acquired in scanning mode show dislocations, dislocation walls (white
350 arrow in **f** and **i**) and subgrains (≤ 200 nm in size, **f**). The PSZ is formed by crystalline material as
351 shown by the diffraction pattern (inset in **f** and **h**). Material abbreviations: Calcite (Cal), Halite (Hl),
352 Dolomite (Dol) and Olivine (Ol).

Figure 4 | Mechanical data in Arrhenius space. **a**, data presented in Figure 1 are rearranged here in an Arrhenius space (natural logarithm of shear stress as a function of the inverse of calculated temperature). **b**, when the fault strength is weak, the mechanical data of each experiment fall on a material-dependent, characteristic straight line. The best-fit equation is shown on the graph for each material. The inset shows mechanical data of Stage III of melt lubrication experiments performed on gabbro, data from Nielsen *et al.*²³.

Methods

Apparatus and sample assembly. The frictional properties of rock powders were tested using a Low to High Velocity Rotary shear apparatus (LHVR, model MIS-233-1-77, Marui & Co., Ltd Company, Osaka, Japan). This machine simulates the development of a narrow fault PSZ at shallow crustal conditions (up to ~2 km in depth). Due to the rotary configuration of the apparatus, it is possible to perform experiments with an arbitrary amount of slip.

The apparatus is housed in a rigid loading frame of steel plates arranged in a vertical configuration and is composed of two vertical shafts, on which the sample assembly is mounted. The upper shaft is connected through a gearbox to an electric servo-controlled motor (11 kW), which outputs a maximum rated torque of 70 Nm and maximum revolution rate of 1500 rpm. The revolution rate and the cumulative rotation angle are measured by a tachometer and a pulse counter (3600 pulses per full rotation), respectively, mounted on the upper shaft. The apparatus can accelerate to the maximum revolution rate (1500 rpm) in 0.277 – 0.351 s at normal stresses of 25 MPa, depending on the tested material (the numbers refer to calcite and olivine powders, respectively). The axial load is applied to the lower main shaft by a pneumatic piston (Bellofram type cylinder) with an 82 mm stroke and maximum thrust of 10 kN. The axial load system is equipped with a high-precision air regulator to automatically correct the load fluctuation during the experiment. Axial load is measured using a compression load cell with a rated output of 2 mV/V \pm 0.5% and resolution of \pm 5 kN.

The axial displacement values are measured using a high sensitivity displacement gauge (strain gauge type) with a capacity of 10 mm and rated output of 5 mV/V \pm 0.1%. Axial displacement resolution is \pm 2 μ m. Torque values are measured by two compression load cells (strain gauge type), which are activated by a torque bar fixed to the lower shaft. The load cell capacity is 1 kN, with a rated output of 2 mV/V \pm 0.5%. Torque cell resolution is \pm 0.5 N.

The sample assembly consists of two hollow cylinders (external radius of 12.5 mm and internal radius of 5.25 mm) sandwiching a layer of gouge (1 g, grain size 63 – 90 μm). The cylinders are made of titanium-vanadium alloy (Ti-alloy, Ti90Al6V4⁴⁷), which is chosen as it has similar thermal properties (thermal conductivity of 5.8 Wm⁻¹K⁻¹) to common rocks. The base of each cylinder that is in contact with the gouge layer is machined with a crosshatch pattern of grooves (500 μm deep), to force shear localisation within the gouge layer. A Teflon cylinder and a Teflon ring tightly fastened by a hose clip, are mounted to prevent the internal and lateral extrusion of the gouge, respectively, during the experiments.

Given the cylindrical shape of the stainless steel cylinders, the slip rate (v) is variable across the sample. A reference radius of 8.33 mm is chosen to calculate slip and tangential slip rate of the material. The temperature rise is calculated using a simple mono-dimensional equation for heat diffusion⁴⁸ in non-adiabatic conditions (see Supplementary Section V for a detailed overview):

$$\Delta T = \frac{1}{2\rho c_P \sqrt{\pi\kappa}} \int_0^t \frac{\tau_v(t')v(t')}{\sqrt{t-t'}} dt' \quad (4)$$

where τ_v is the shear stress, v is the velocity, ρ is the rock density, c_P is the specific heat, κ is the thermal diffusivity, Φ is the heat flux and t is time.

Microstructural analysis. Samples are carefully recovered after each run and prepared for microstructural analysis (see Supplementary Section I for further information). Cross-sections were studied using a FEI Helios Dual Beam Nanolab 600 scanning electron microscope (SEM) at the Department of Physics of Durham. Images were acquired in back-scattered (BS) and fore-scattered (FS) modes. BS is operated using the through-the-lens acquisition system on samples coated with graphite (< 30 nm). FS is operated on uncoated specimens tilted at 70° using a 4 Quadrant KE Development FS imaging control detector. FS technique is best used for detailed microstructures as it produces good contrast along the grain boundaries.

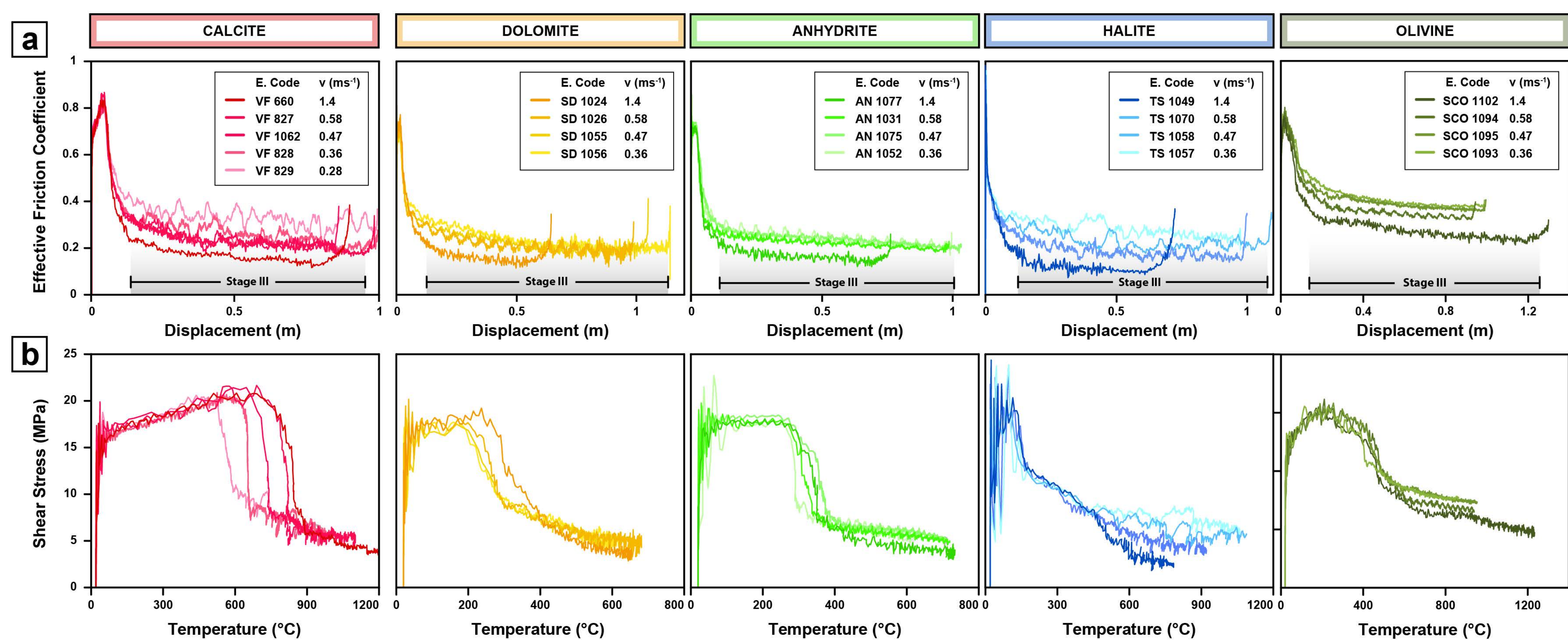
FEI SEM was also used to prepare thin foils – carved with ion milling from specific locations of SEM-prepared samples – for transmission electron microscopy (TEM). Images were acquired on a JEOL 2100F FEG TEM at the Department of Physics of Durham using scanning (STEM) mode.

Data availability. Data within the manuscript and its Supplementary Information are available from the corresponding author upon request.

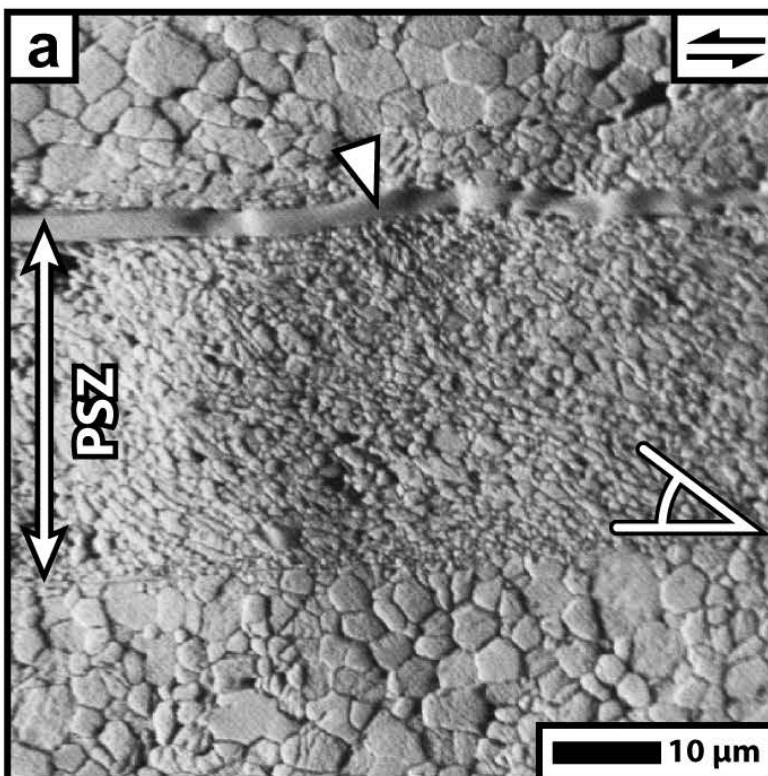
47. Yao, L., Ma, S., Platt, J. D., Niemeijer, A. R. & Shimamoto, T. *The crucial role of temperature in*

385 *high-velocity weakening of faults: Experiments on gouge using host blocks with different thermal*
386 *conductivities*. *Geology* 44, 63–66 (2016).

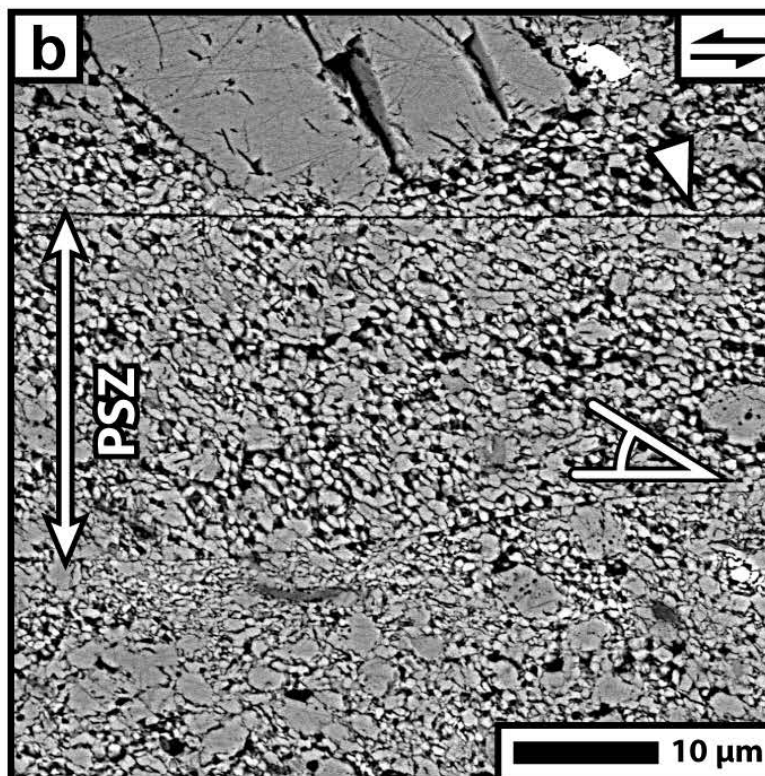
387 48. Rice, J. R. *Heating and weakening of faults during earthquake slip*. *J. Geophys. Res. Solid Earth*
388 111, B05311 (2006).



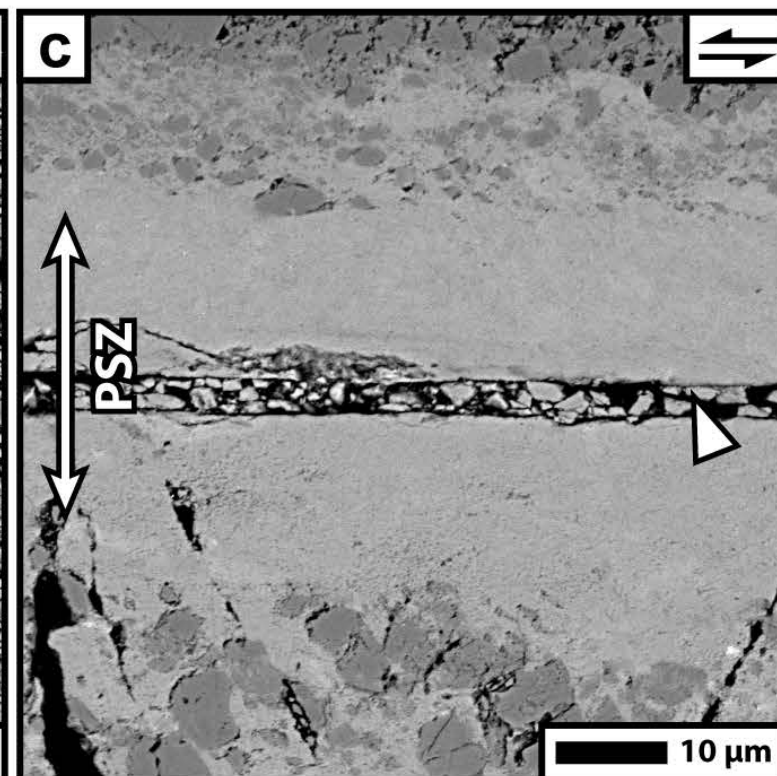
CALCITE (VF 660)



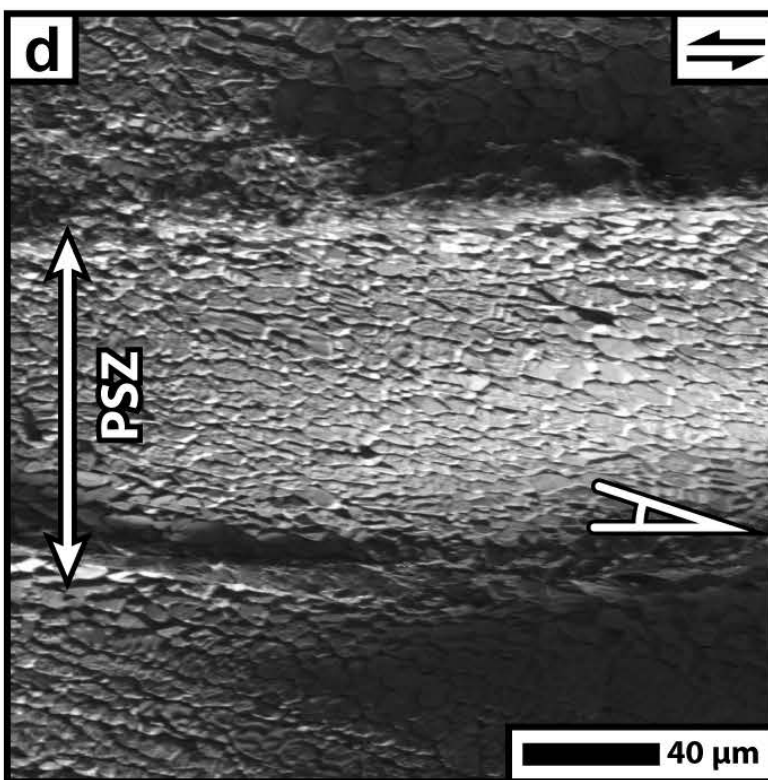
DOLOMITE (SD 1026)



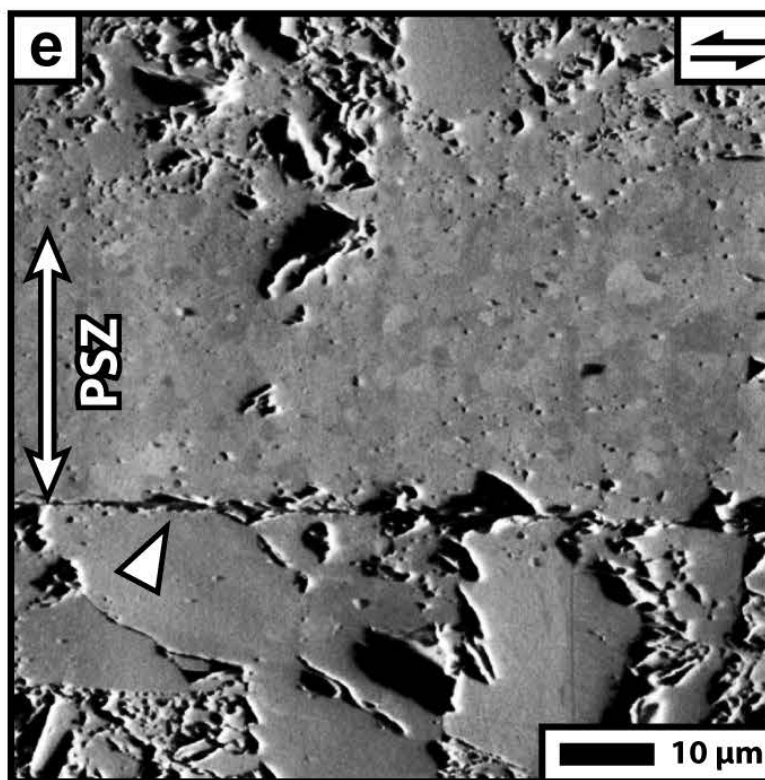
ANHYDRITE (AN 1031)



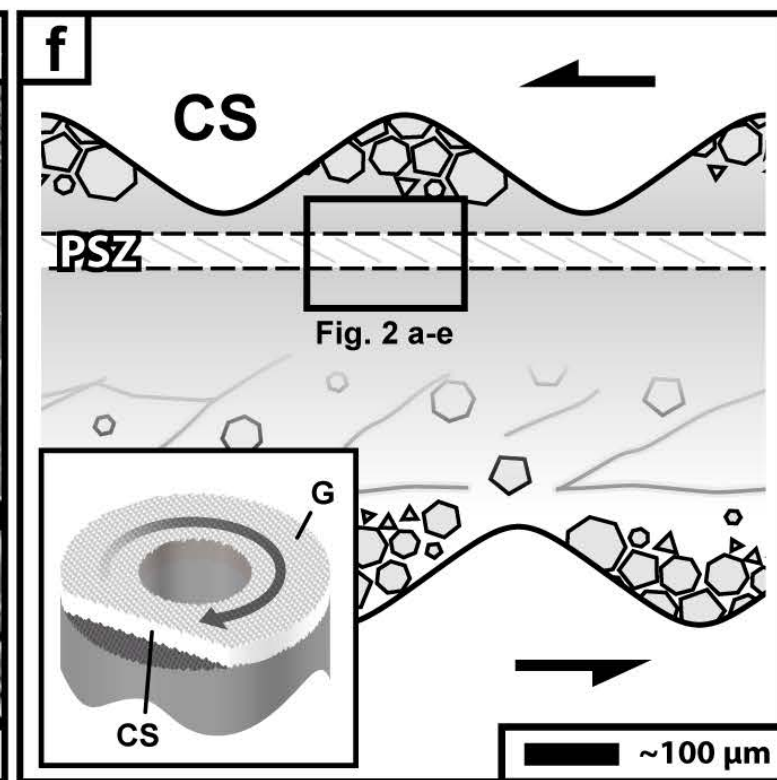
SODIUM CHLORIDE (TS 1049)



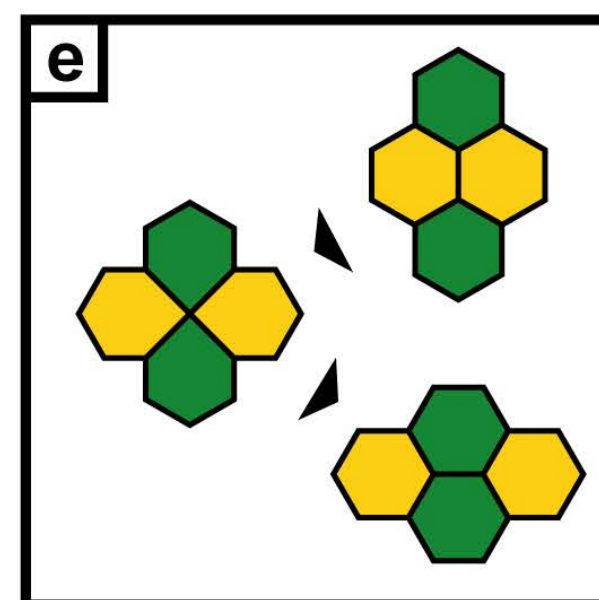
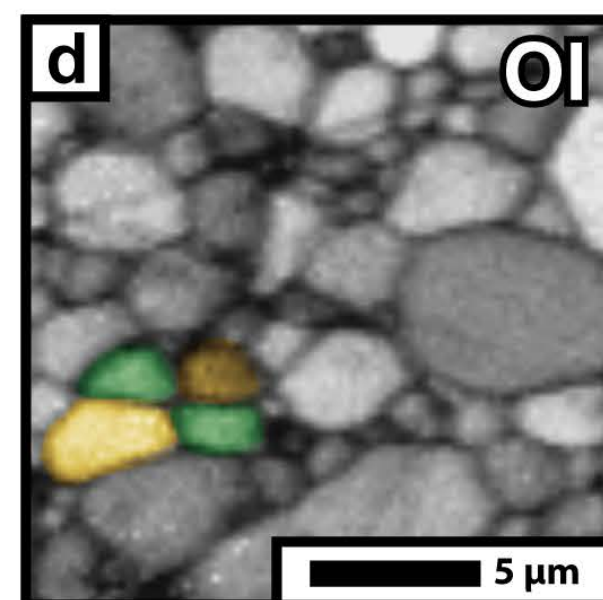
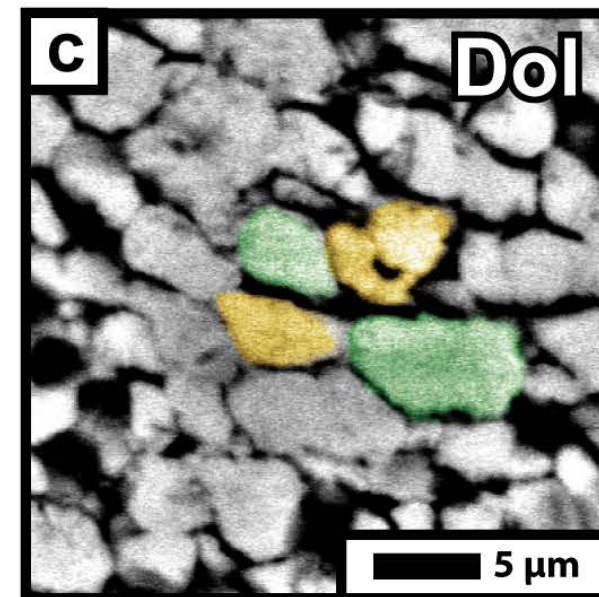
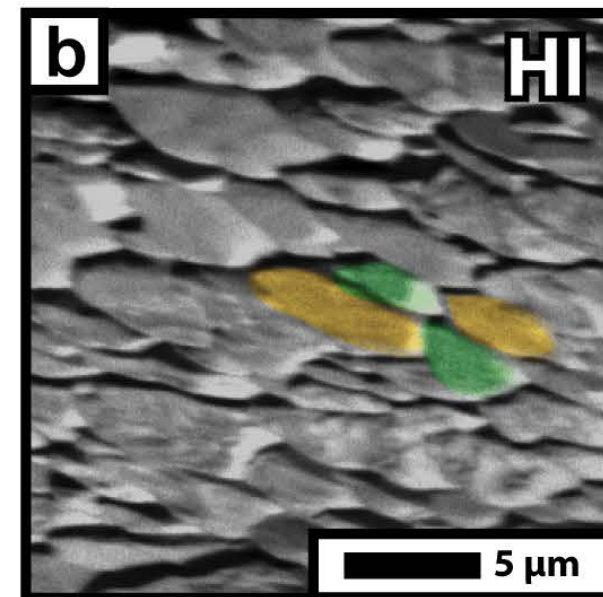
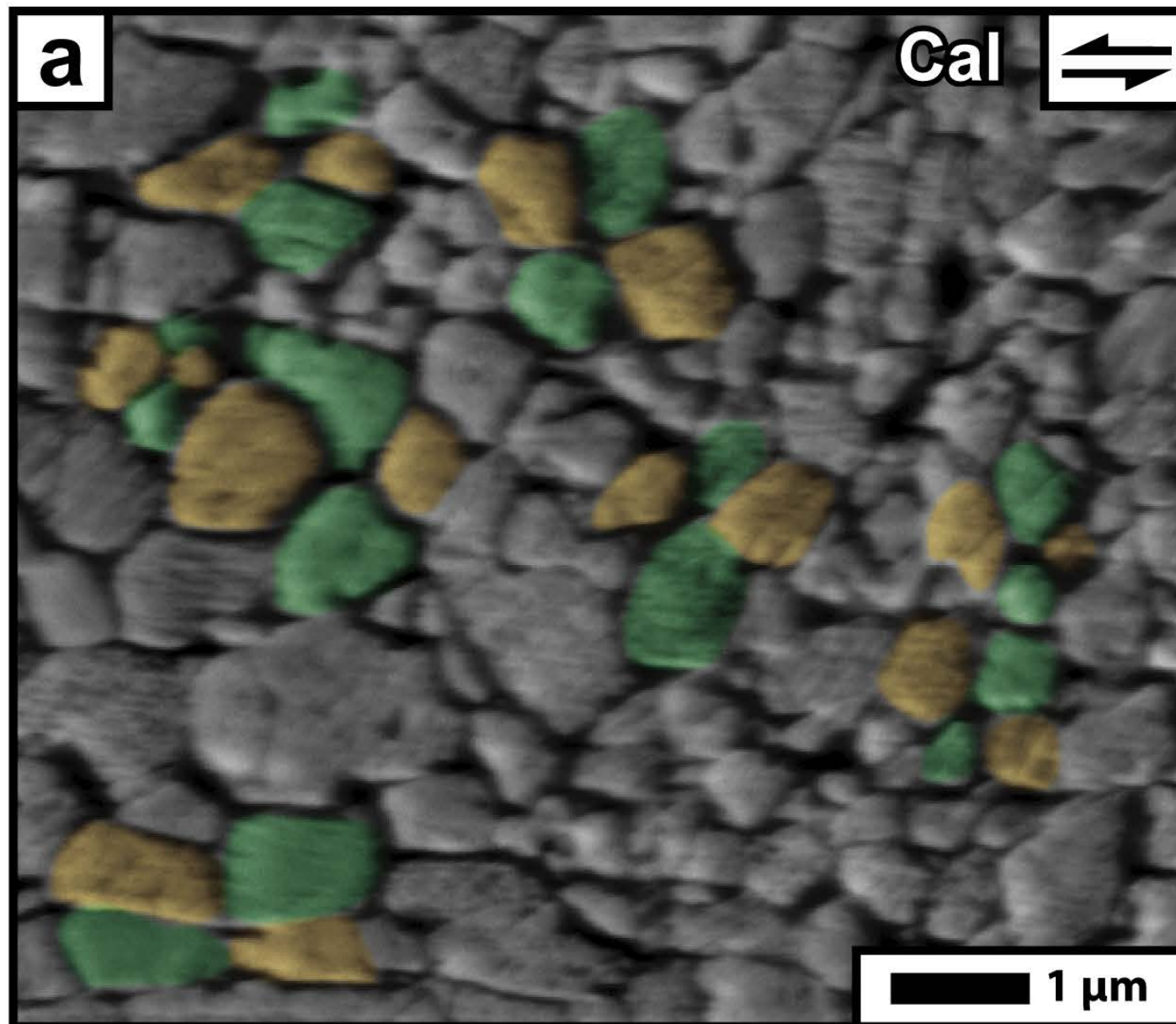
OLIVINE (SCO 1095)



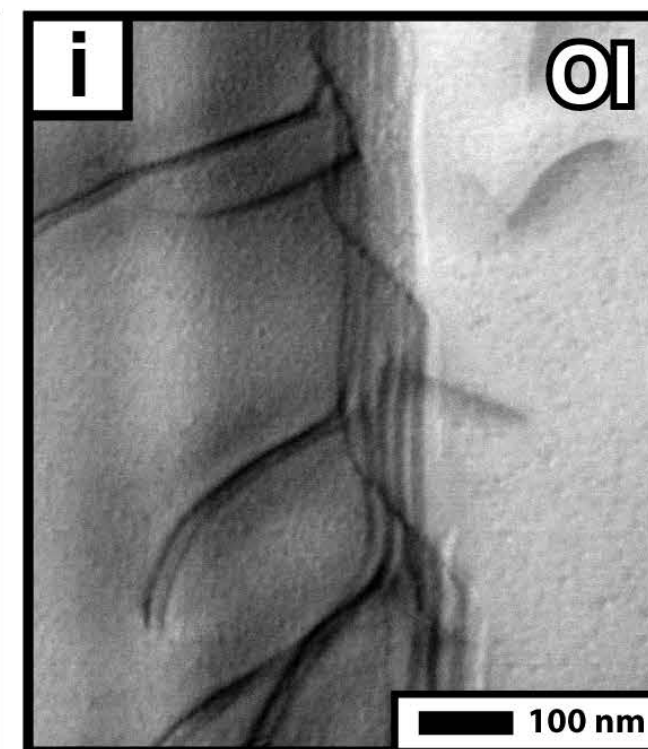
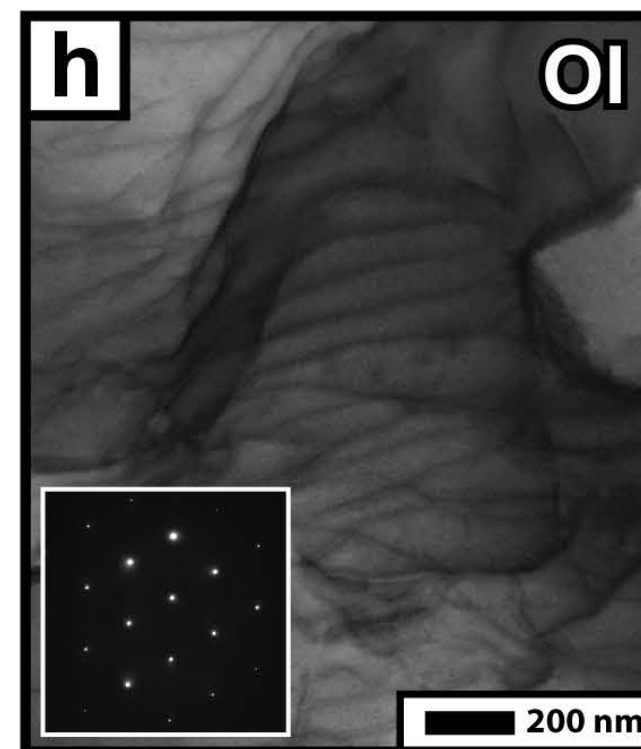
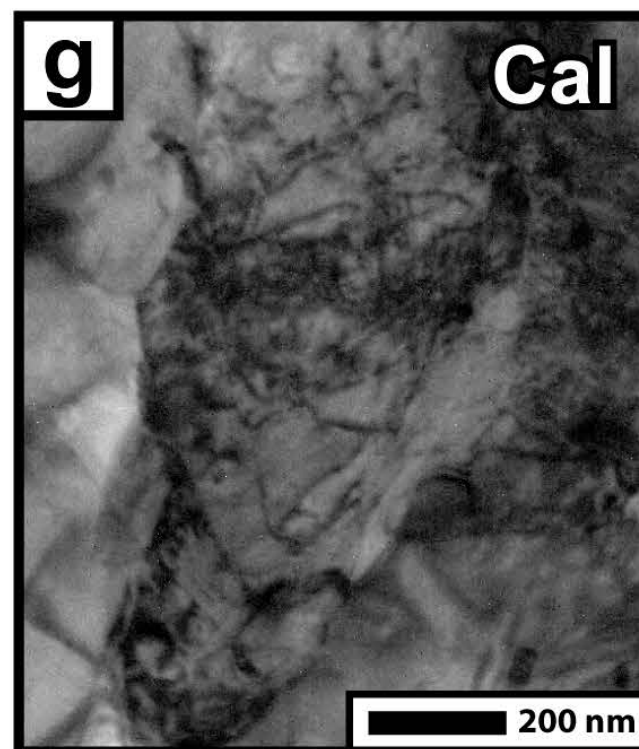
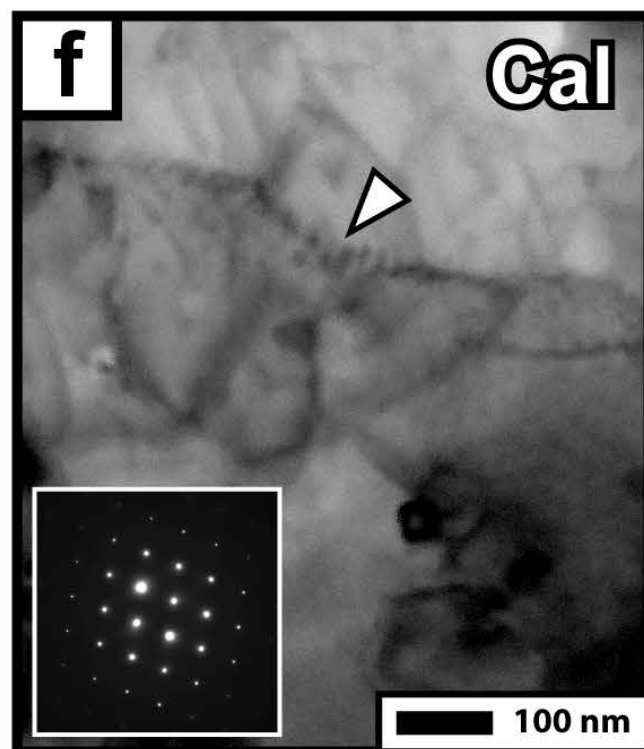
PSZ LOCATION

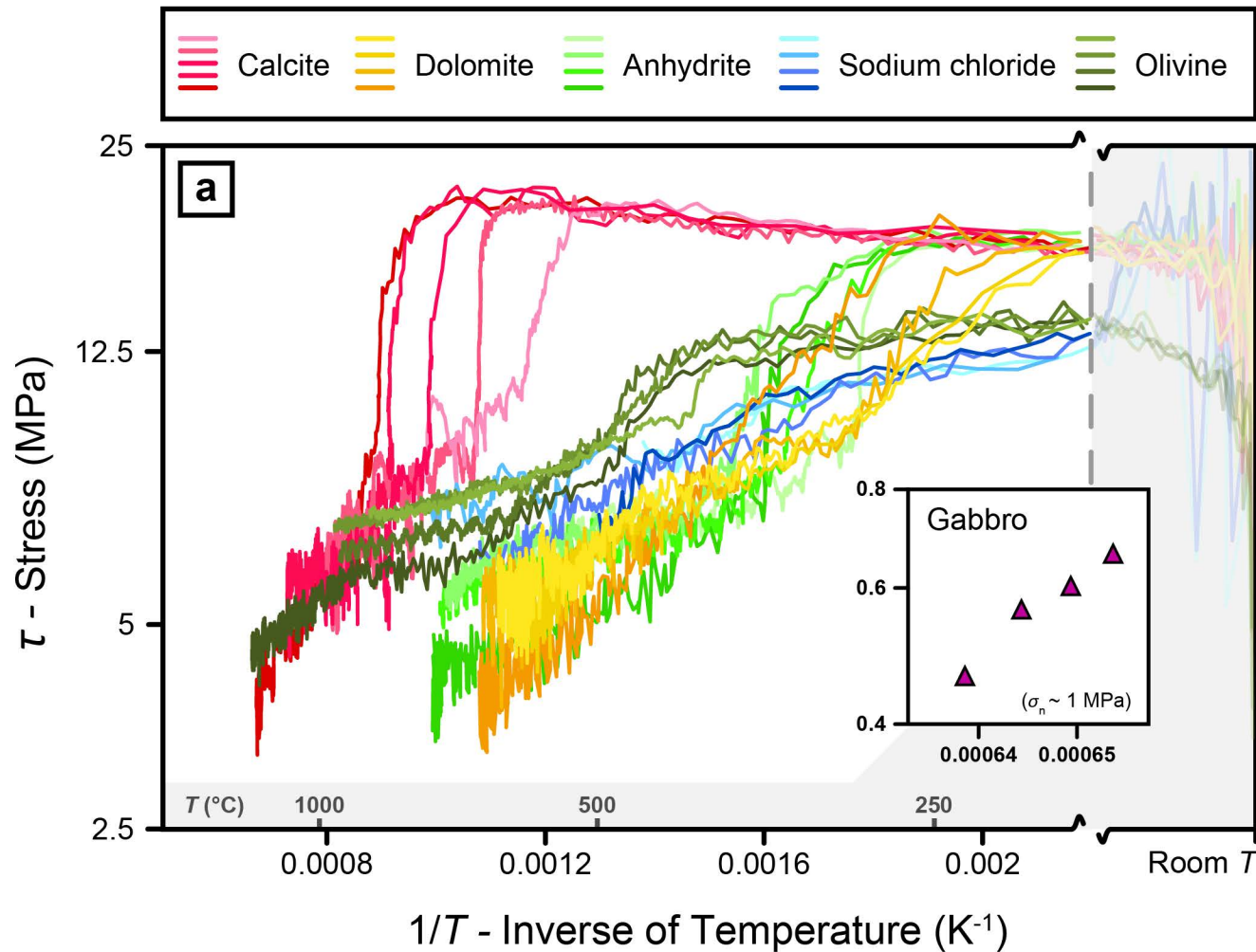


Grain Boundary Sliding

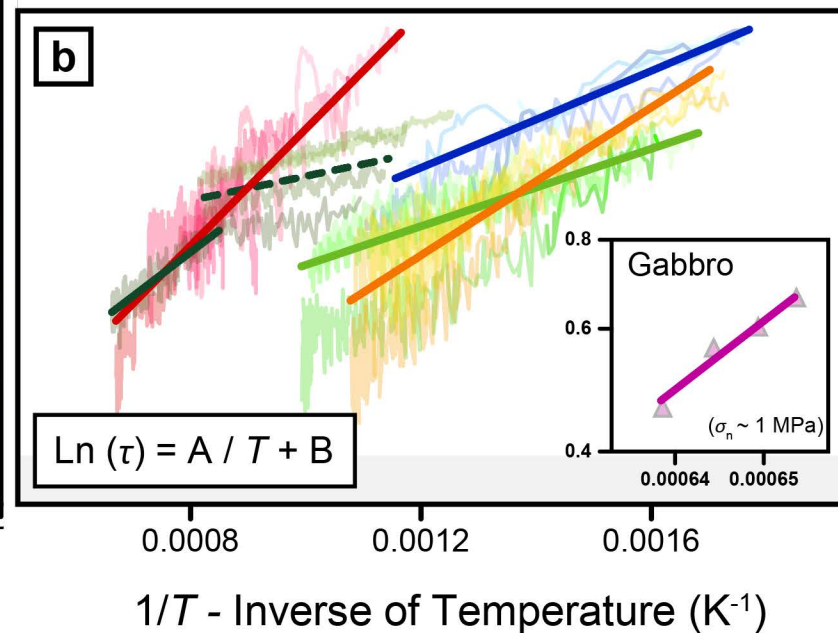


Dislocation Creep





Best Fit	Calcite	$\ln(\tau) = 1950.804/T + 0.110$
	Dolomite	$\ln(\tau) = 1238.735/T + 0.151$
	Anhydrite	$\ln(\tau) = 648.712/T + 0.957$
	Sodium chloride	$\ln(\tau) = 815.215/T + 0.951$
	Olivine 1 (average)	$\ln(\tau) = 400.117/T + 1.590$
	Olivine 2 (1.4 ms^{-1})	$\ln(\tau) = 1472.210/T + 0.570$
	Gabbro	$\ln(\tau) = 22459.330/T - 15.090$



Coseismic fault lubrication by viscous deformation

Giacomo Pozzi^{1*}, Nicola De Paola^{1*}, Stefan B. Nielsen¹, Robert E. Holdsworth¹, Telemaco Tesei²,
Manuel Thieme³ and Sylvie Demouchy³.

¹Department of Earth Sciences, Rock Mechanics Laboratory, University of Durham, Durham, DH1 3LE, UK.

²Department of Geosciences, University of Padova, Via Gradenigo 6, I-35131 Padova, IT.

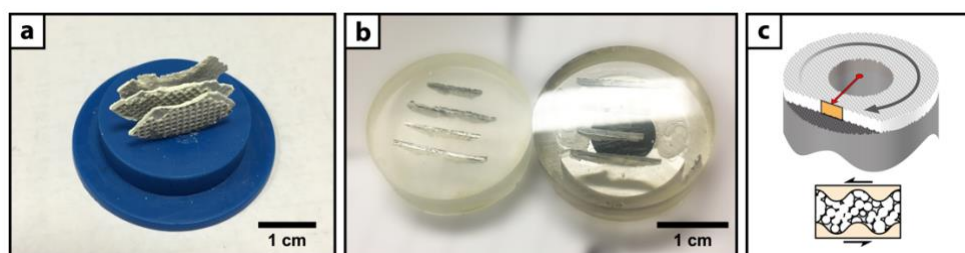
³Geosciences Montpellier, CNRS & Université de Montpellier, UMR5243, 34095 Montpellier, FR.

*Corresponding Authors: giacomo.pozzi@ingv.it, nicola.de-paola@durham.ac.uk

Supplementary Section I | Recovery of microstructures

Samples are carefully recovered after each high velocity friction experiment for microstructural analysis. To understand deformation processes and slip localization during a friction test, it is crucial to recover the full thickness of the experimental material (Supplementary Figure 1). Due to the common formation of mirror-like surfaces (MSs), samples split easily along them¹ when recovered from the metal cylinders (Supplementary Figure 14). When this happens, it means that the full thickness of the deformed sample cannot be recovered, potentially undermining the full characterisation of the inner architecture of the slip zone. Therefore, the procedure of sample removal was carried out as carefully as possible trying to preserve the entire thickness of material located between the metal cylinders. First, the confining Teflon ring is loosened and slid down one of the cylinders, while the sample is still mounted on the machine. The normal load is then removed slowly until the two cylinders separate. After removal from the machine, the sample is collected with tweezers and carefully stored. This method, when carried out successfully, allows microstructural observations of the entire thickness of the deformed sample, including full imaging of the architecture of the entire slip zone (Supplementary Figure 1). We emphasize that recovery of the full width of the sample from high-velocity experiments is exceedingly difficult and only rarely documented in the existing literature.

The largest sample chips recovered after the experiments were mounted vertically using cyanoacrylate superglue in a cylindric mould and embedded in epoxy (Supplementary Figure 1a). A high viscosity resin (e.g., epoxy) was used in order to avoid further damage to the microstructures (like splitting along MSs by capillarity). Epoxy mounts obtained this way were then machined with a grinder polisher using sand paper to expose a representative cross-section of the embedded chips. The section is chosen at a distance equal to the reference radius (halfway between the sample contacts with the internal and external Teflon seals), parallel to the slip direction and perpendicular to the rotation plane (Supplementary Figure 1c). The cut surface was lapped with progressively finer diamond paste (6, 3, 1 and 0.25 μm). Each step required between 5 to 10 minutes to be completed by the user (Supplementary Figure 1b). Given the frailty of the rocks analysed, longer polishing sessions generally resulted in badly damaged surfaces.

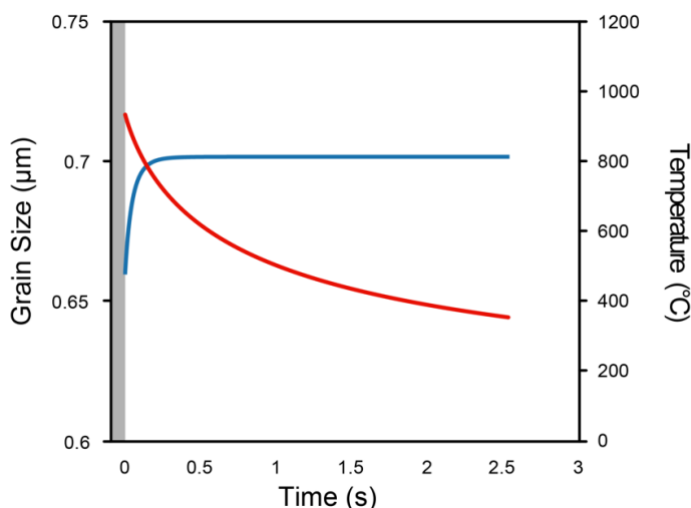


Supplementary Figure 1 | Sample preparation: **a**, vertical mount of the sample chips on the mould base, prepared to be embedded in epoxy; **b**, sample chips embedded in epoxy mount and cut at the reference radius, before (left) and after (right) polishing; **c**, schematic of the position of the cross-sectional area used for microstructural analysis (orange area); the reference radius is represented by a red arrow.

Satisfying results were achieved using this procedure for calcite and olivine samples. Sections of sodium chloride samples were flattened using humid lens cleaning paper and a single lapping with 1 μm diamond suspension. In anhydrite and dolomite samples, our attempts have been less successful. In anhydrite, the small grain size and low indentation hardness did not allow for long polishing sessions. Polished surfaces were therefore not suitable for high-resolution imaging, mostly due to charging effects (drift of the electron beam) caused by the small grain sizes and enhanced topography. Dolomite samples, despite having a tightly-packed, fine-grained texture, are less cohesive than calcite samples. Polishing of dolomite cross-sections resulted in continuous plucking-out of grains well illustrated in Supplementary Figure 6 (not to be confused with porosity, which is low within the PSZ).

Supplementary Section II | Static grain growth and post-mortem microstructures

A severe limitation when coupling mechanical data and microstructural observations can potentially arise due to the post-mortem nature of microstructures. In other words, the fabrics (or texture) developed within the principal slip zone (PSZ) at dynamic conditions might change through the stages of deceleration of the machine to arrest, including static growth due to the residual heat dissipating after the end of the experiment and brittle damage during unloading and removal of the sample. While it is difficult to constrain the evolution during deceleration (dynamic conditions), static grain growth can be estimated. Using the well-known equation by Covey-Crump² for calcite, we observe that microstructures and textures are unlikely to be overprinted by annealing at the end of the experiment in calcite (Supplementary Figure 2). In fact, using the experimental cooling curve at static conditions (starting at the end of the experiment run, see Supplementary Information Section VI), the estimated grain growth to target (an average of 0.7 μm in the VF 660 annealed PSZ¹) is ~ 40 nm. This corresponds to a grain growth of $\sim 6\%$ of the equivalent radius, which is not sufficient to overprint the existing textures.



Supplementary Figure 2 | Static grain growth within the PSZ of VF660 (target of 700 nm, observed in post-mortem samples), calculated using the temperature decay after the cessation of slip. When temperature drops below 700 $^{\circ}\text{C}$, grain growth becomes irrelevant at the timescale of non-isolated cooling to room temperature. Grain growth parameters for calcite used here are as reported in De Paola *et al.* (2015)³.

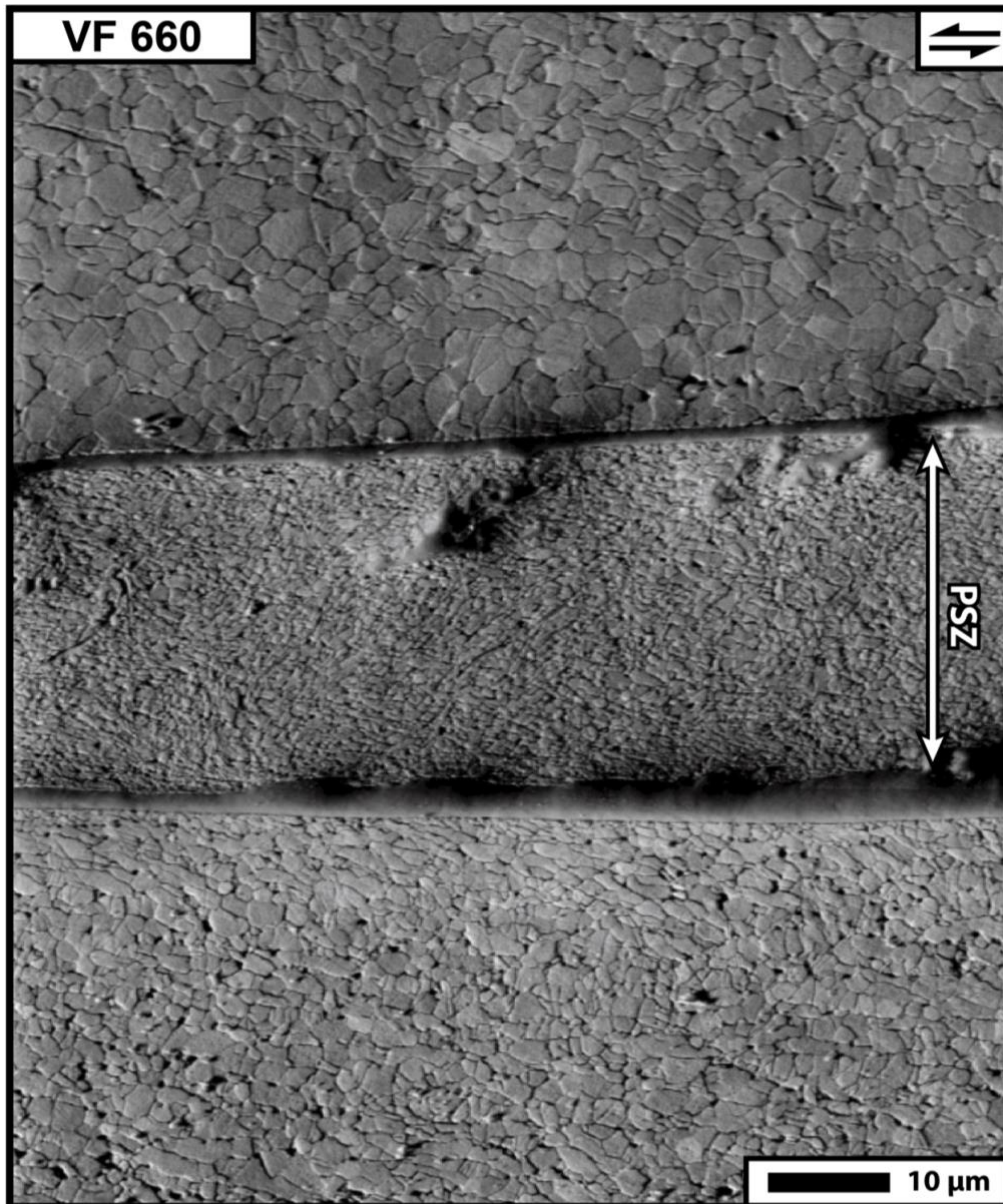
In the case of olivine, where the kinetics of diffusion are extremely slow in the temperature range, grain growth is expected to be negligible for the run durations used here. Previous studies⁴ showed that fine grained ($< 2 \mu\text{m}$) aggregates of olivine do not experience significant grain growth ($< 1 \mu\text{m}$ after 20 h at 1270°C , from hot press experiments).

Finally, some degree of brittle overprint is ubiquitous during deceleration of the machine resulting in variable sample fragmentation. Commonly (e.g. Supplementary Figure 3), brittle overprint occurs by splitting along mirror surfaces (but not always, e.g. Supplementary Figure 7). However, this brittle overprint is easily recognized and does not destroy the microstructure and texture developed at dynamic conditions¹. We therefore conclude that PSZ microstructures presented here are representative of those formed during Stage III weakening.

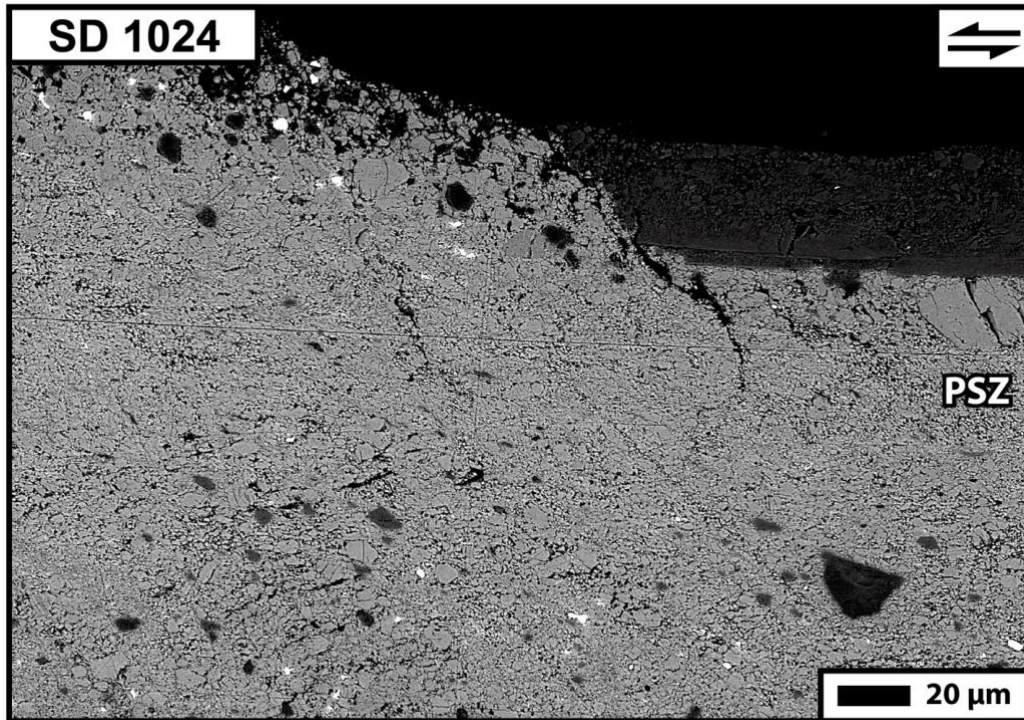
Supplementary Section III | Microstructures

Scanning electron microscope (SEM) images

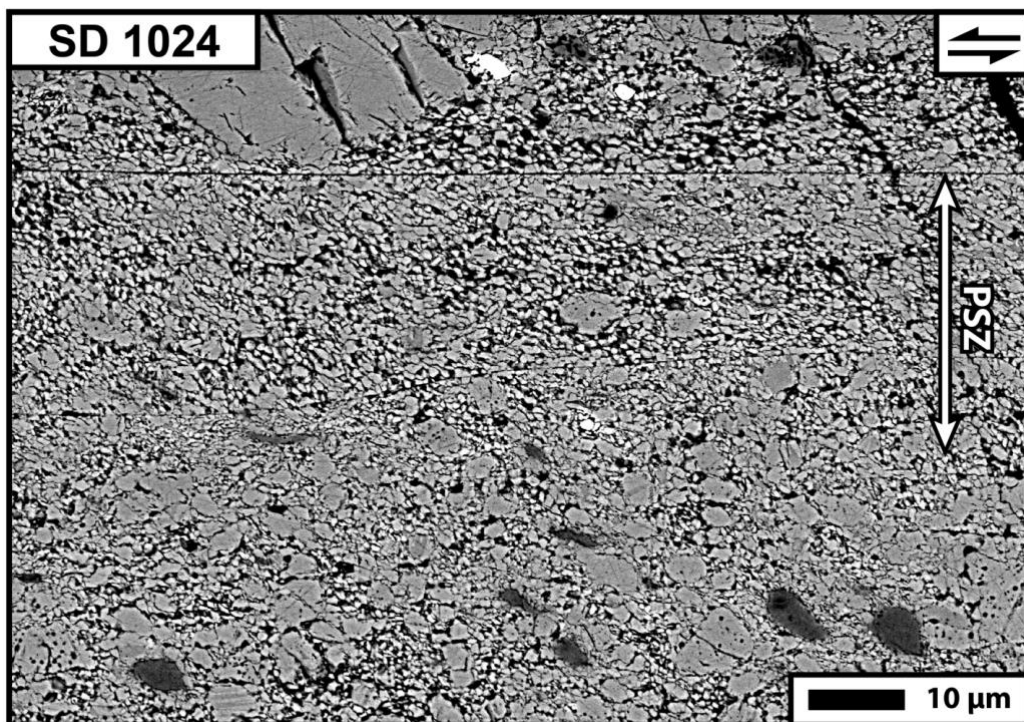
In the following, we give an overview and details of principal slip zones recovered from the high-velocity friction tests. Representative sections are selected to show all lithologies examined in the main manuscript.



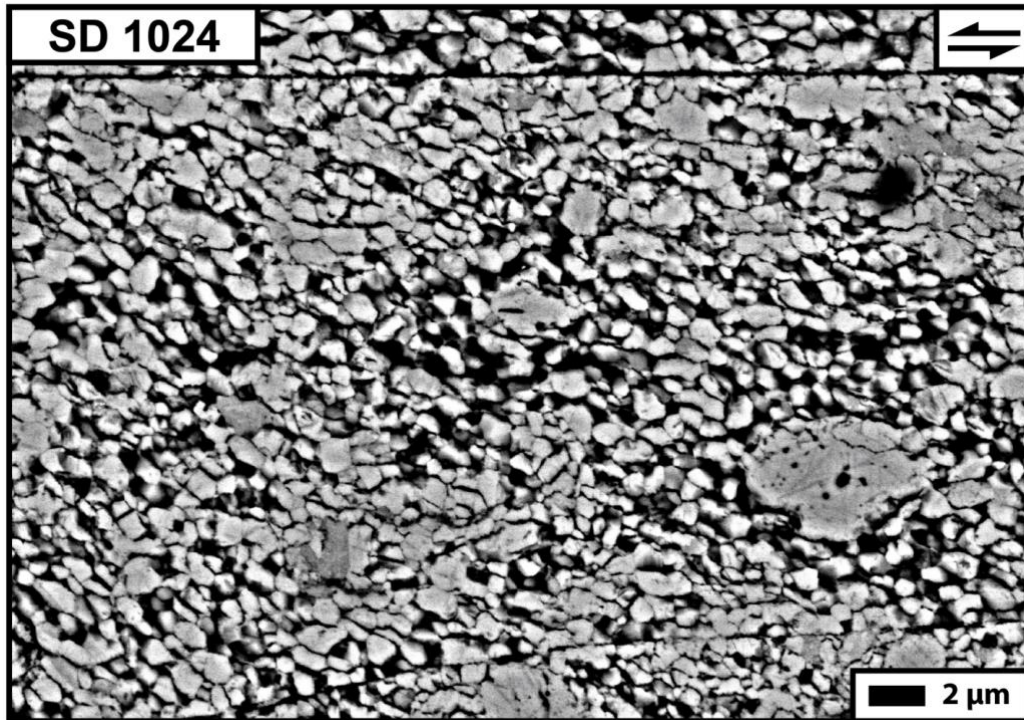
Supplementary Figure 3 | Forward-scattered SEM image of calcite principal slip zone (PSZ, $v = 1.4 \text{ ms}^{-1}$). Note the epoxy infilling thin cracks formed at the PSZ boundary (see Pozzi *et al.*, 2018). Splitting along the mirror follows broadly, but not perfectly (see bottom left edge of the PSZ) the granulometric contrast within the PSZ.



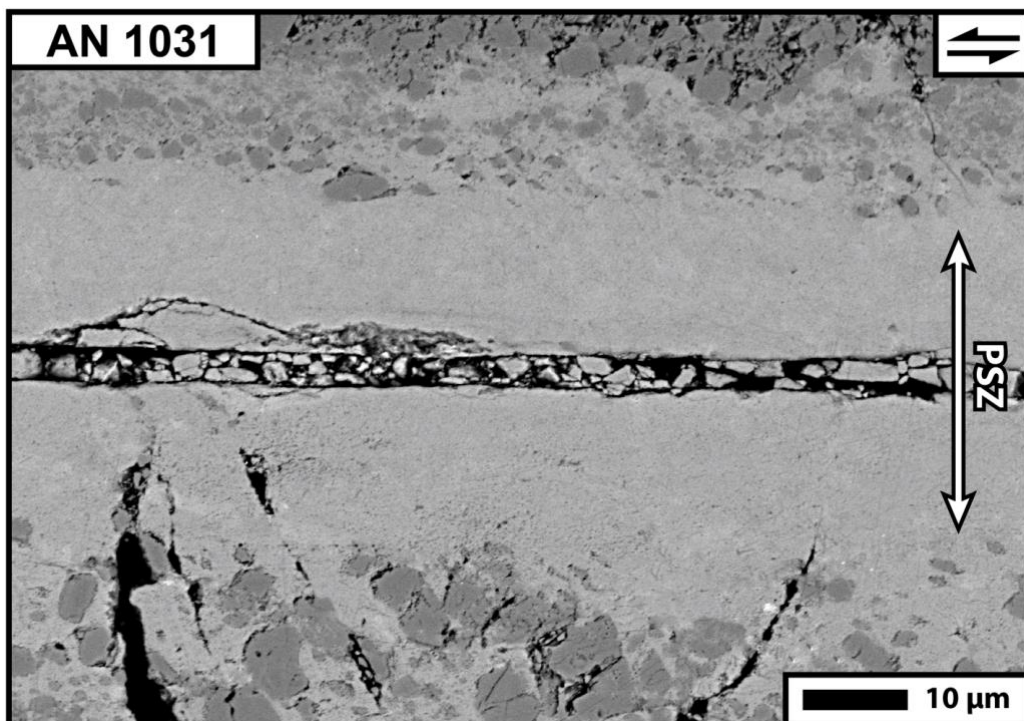
Supplementary Figure 4 | Back-scattered SEM image of dolomite experiment ($v = 0.58 \text{ ms}^{-1}$). The dark area in the upper right corner shows the indentation with the upper cylinder.



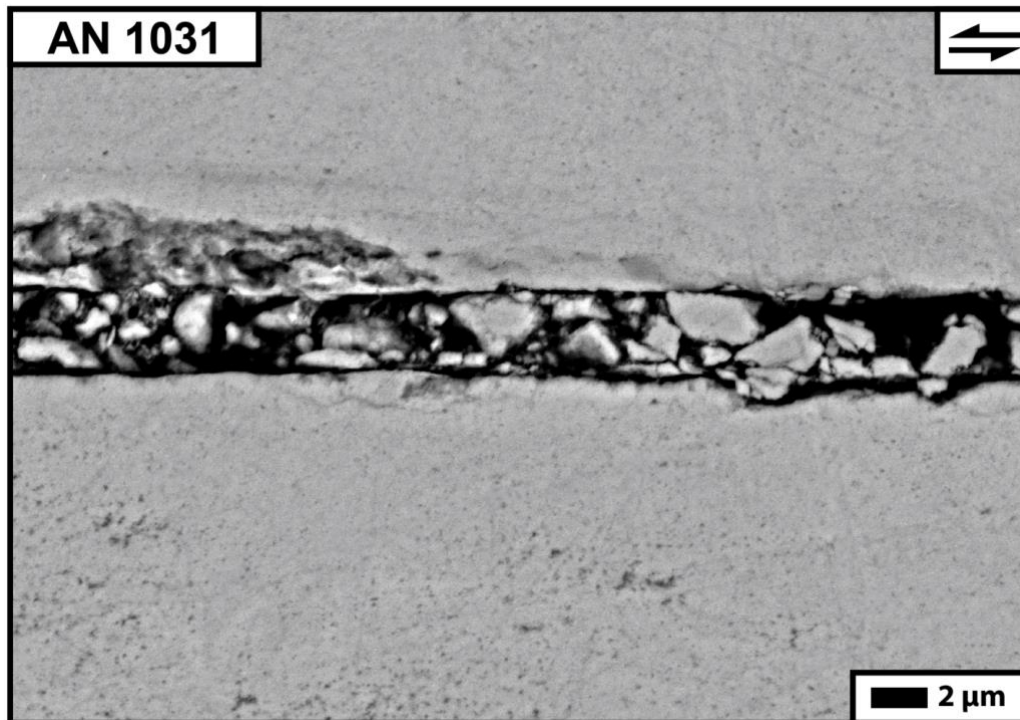
Supplementary Figure 5 | Back-scattered SEM image of dolomite PSZ ($v = 0.58 \text{ ms}^{-1}$). The PSZ is defined by the layer with the smaller average grainsize that also displays an oblique foliation and few surviving prophyroclasts. In the upper part, the through-going fractures are due to late splitting along the PSZ boundaries.



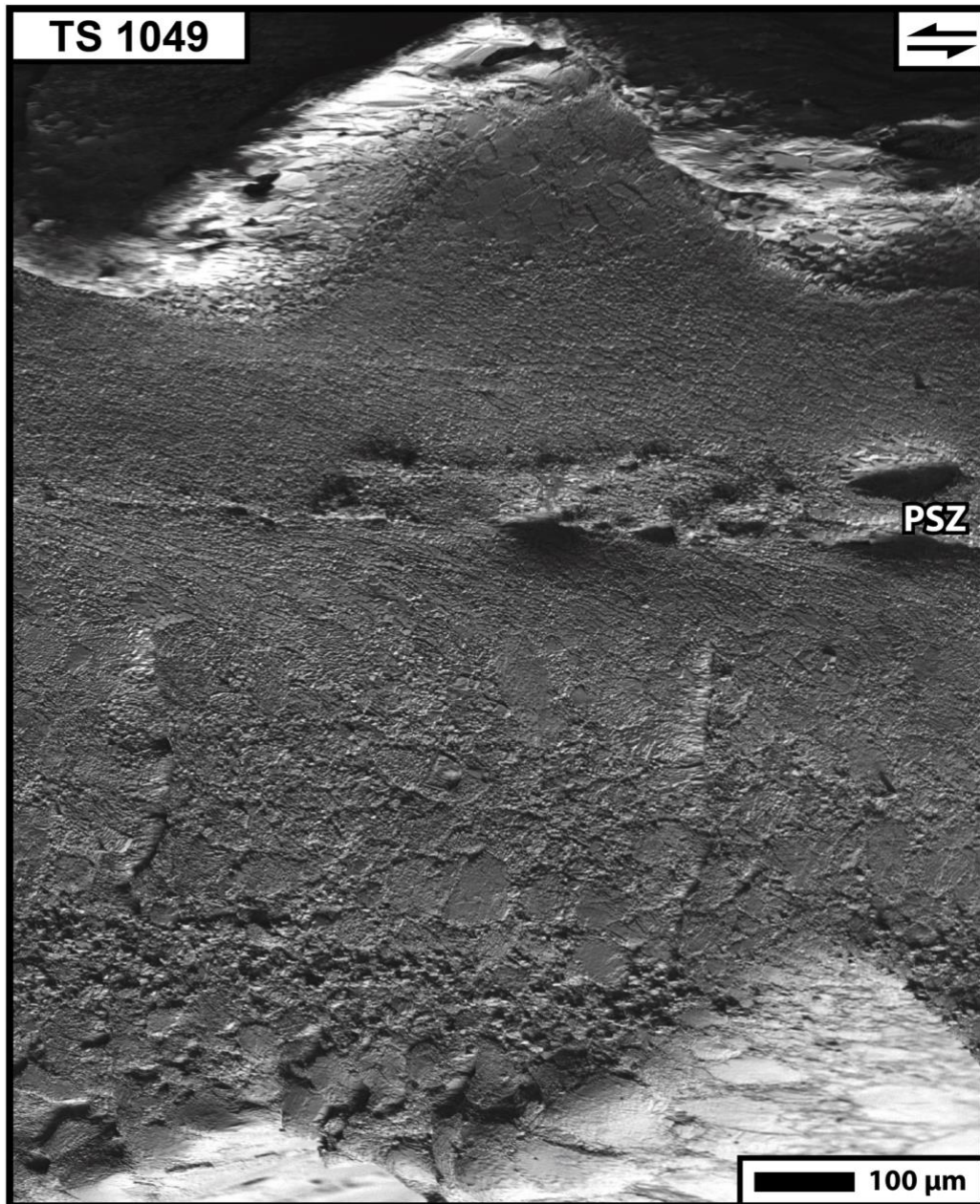
Supplementary Figure 6 | Back-scattered SEM image within the dolomite PSZ ($v = 0.58 \text{ ms}^{-1}$). Grain boundaries are accentuated by late-stage brittle damage. Note the polygonal holes left by plucking-out of grains during sample preparation.



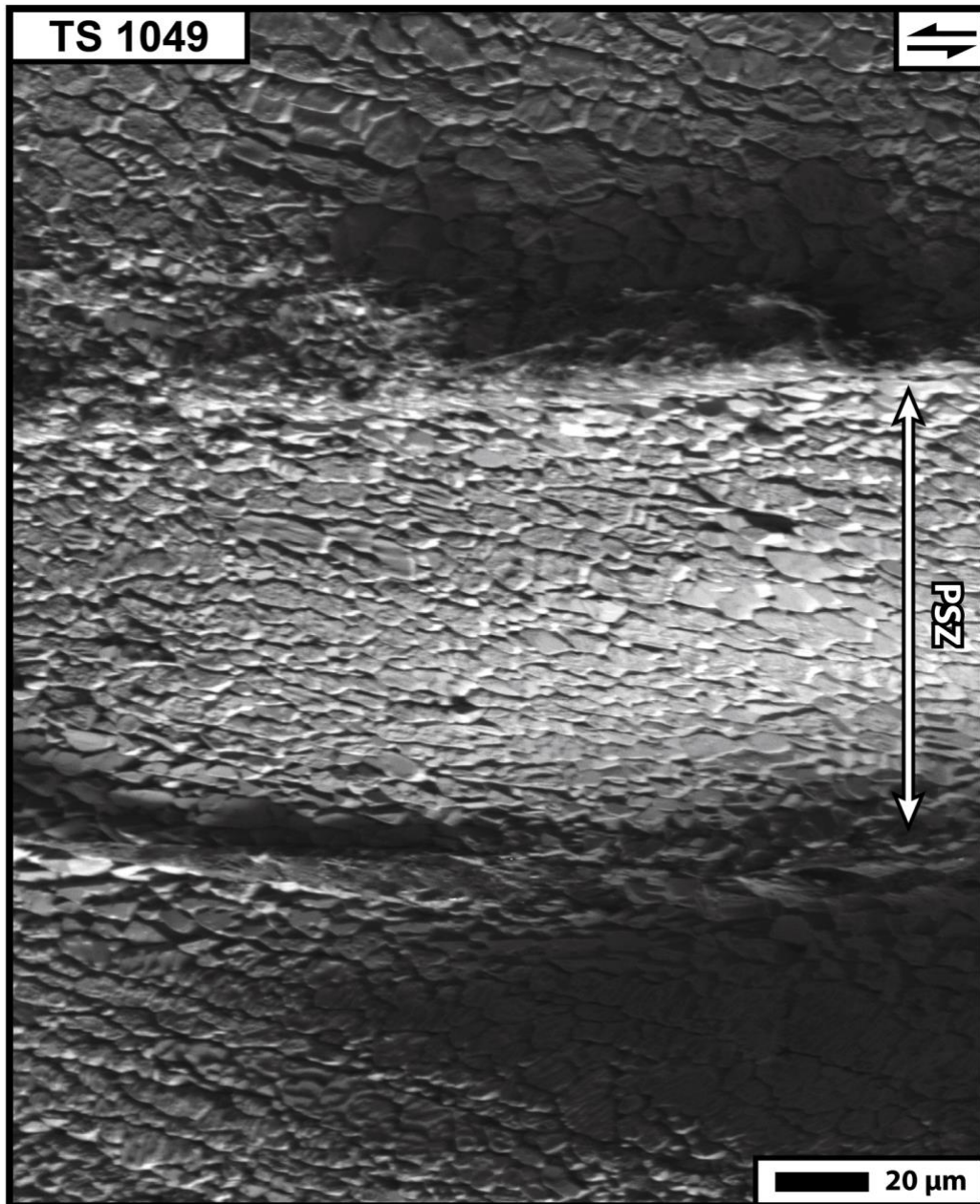
Supplementary Figure 7 | Back-scattered SEM image of anhydrite PSZ ($v = 0.58 \text{ ms}^{-1}$). The PSZ is composed of extremely fine-grained crystals (barely resolvable at this scale) and by incipient oblique foliation.



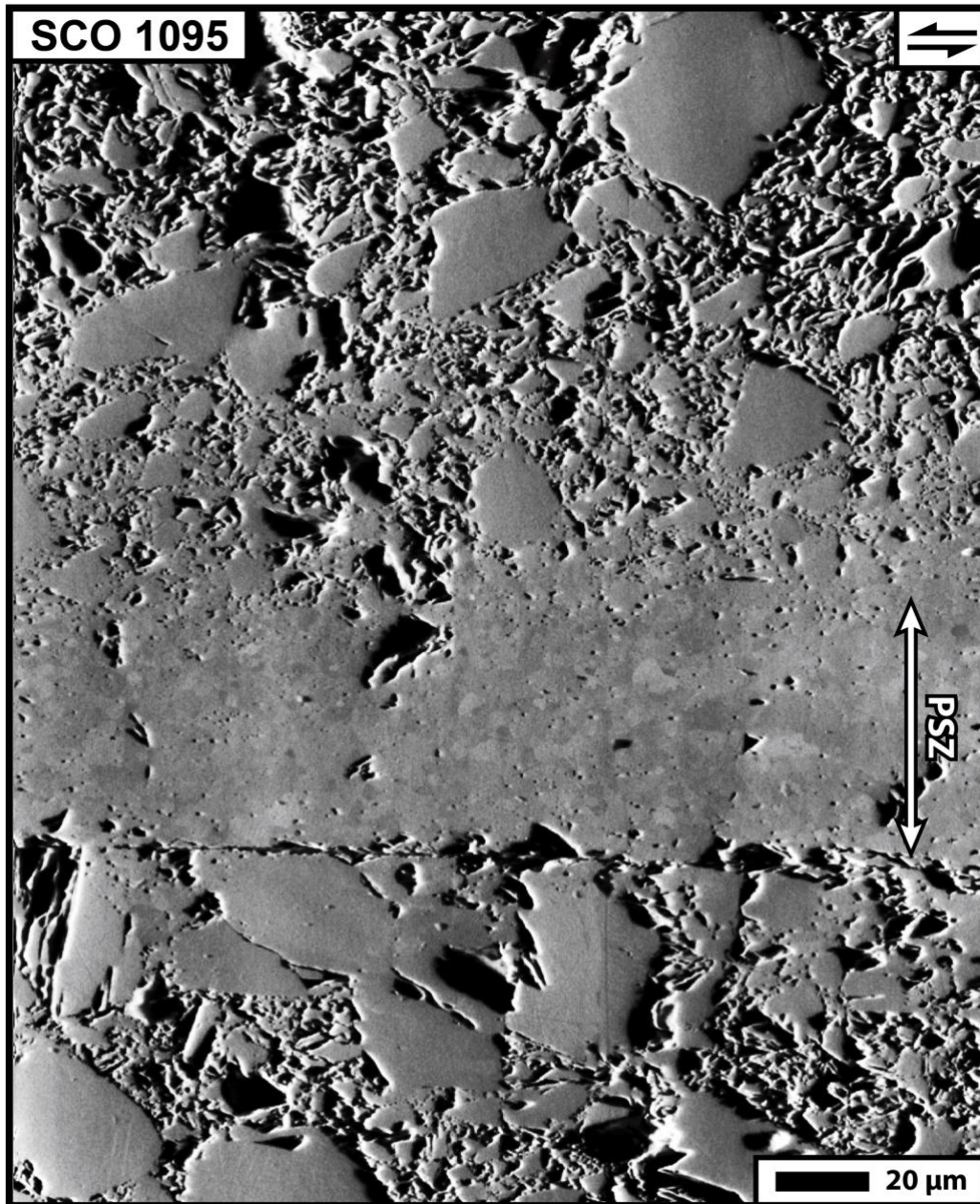
Supplementary Figure 8 | Back-scattered SEM image within the anhydrite PSZ ($v = 0.58 \text{ ms}^{-1}$). In the centre, late stage damage produced during the deceleration stage and decompression occurs. The PSZ is composed of sub-micron size grains with very low porosity.



Supplementary Figure 9 | Back-scattered SEM of sodium chloride experiment ($v = 1.4 \text{ ms}^{-1}$). Note the sawtooth profile of the upper and lower parts of the sample left by the indentation with the upper cylinder. On the lower half of the sample, the large grainsize of clasts is similar to the initial grainsize indicating a low-strain domain. Grain size reduction and homogenisation is observed towards the PSZ. Note also the intensification of the oblique foliation toward the PSZ.

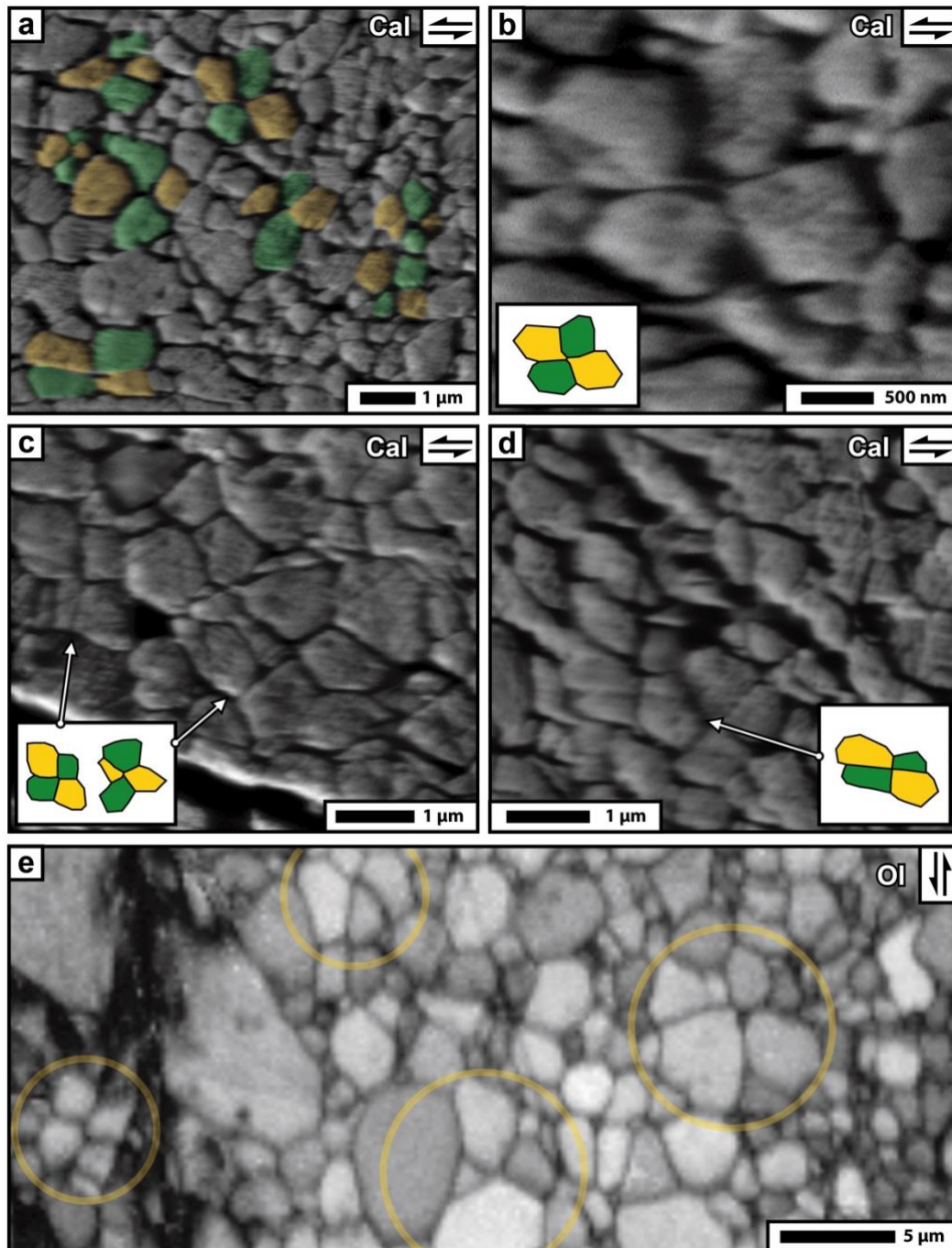


Supplementary Figure 10 | Back-scattered SEM of sodium chloride PSZ ($v = 1.4 \text{ ms}^{-1}$). The PSZ is bounded by a thin, discontinuous layer of material with finer grain size (not resolvable), interpreted as melt patches. The high relief of the grains is due to the effects of water etching during sample preparation.



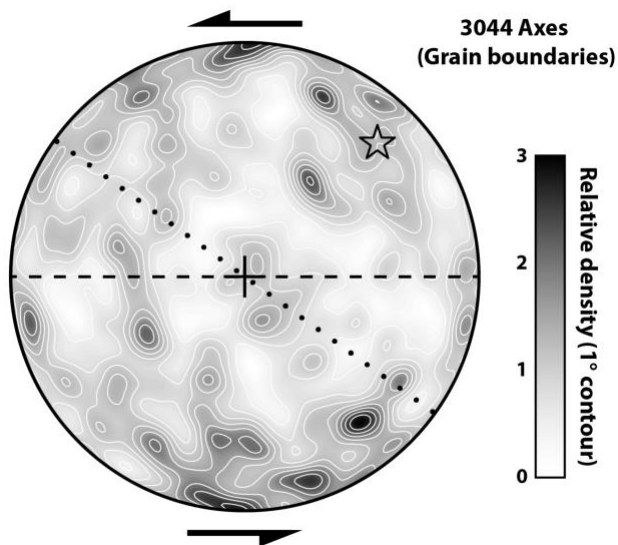
Supplementary Figure 11 | Forward-scattered SEM image of olivine PSZ ($v = 0.47 \text{ ms}^{-1}$). The PSZ is formed by a low-porosity olivine aggregate with a narrow distribution of grain sizes. Grains are visible due to their different crystallographic orientation (different shades of grey). Outside the PSZ, fragmented grains are large and poorly sintered.

Quadruple junctions



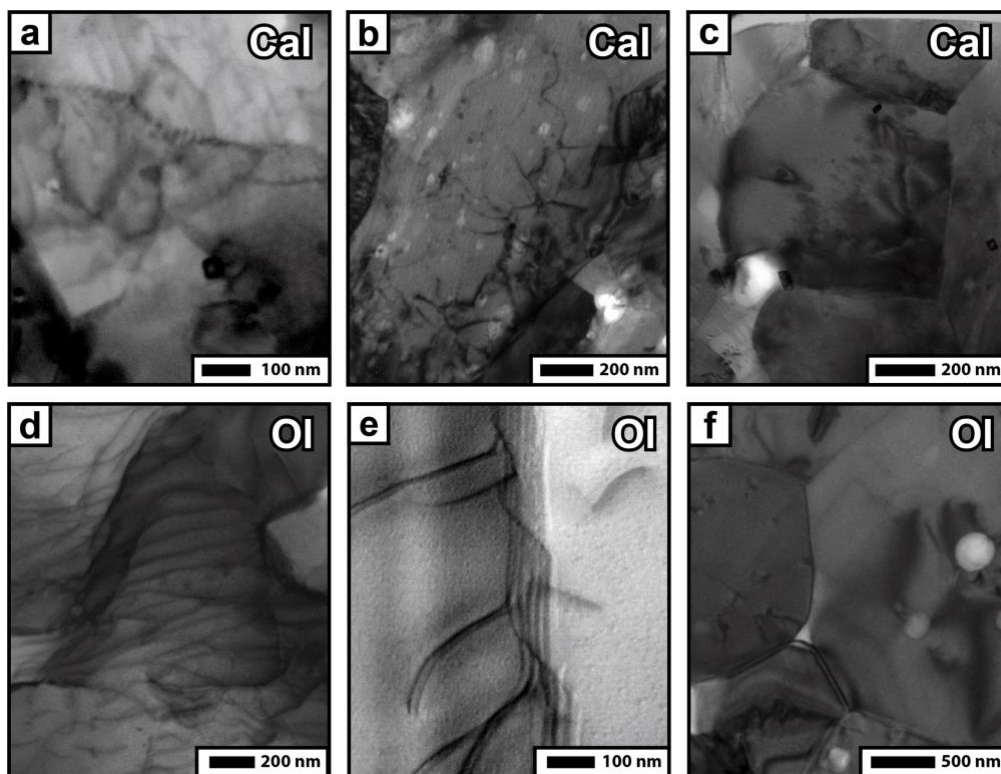
Supplementary Figure 12 | SEM close-up images of quadruple junctions in calcite (a-d, forward-scattered technique) and olivine (e, EBSD band contrast) principal slip zones (PSZs). Groups of four grains displaying quadruple junctions (coloured in green and yellow in calcite, Cal, and circled in olivine, Ol) are common within the PSZs. Grains are diamond-shaped and show alignment of grain boundaries with the shear direction (arrows). These microstructures are typical of grain boundary sliding (GBS, see main text).

Aligned grain boundaries – EBSD data



Supplementary Figure 13 | Pole figure of the orientation of calcite-calcite grain boundaries in the PSZ of sample VF660, obtained with EBSD analysis and using MTEX toolbox^{5,6}. The colour scale shows the relative density of grain boundary axes (contour resolution 1°). The plot shows a relatively higher density of boundaries oriented sub-parallel (axes oriented N-S) to the shear direction (dashed line). There are also distinctive maxima oriented NE-SW (star), corresponding to the boundaries that form the oblique foliation (dotted line). Black arrows indicate the sense of shear.

TEM images



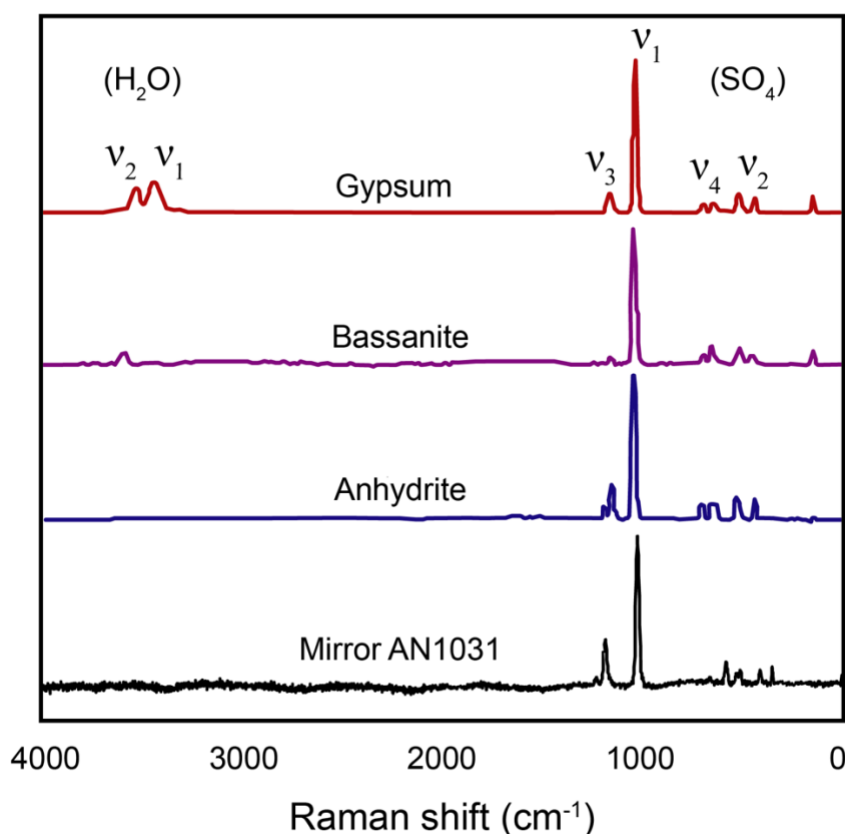
Supplementary Figure 14 | Scanning TEM bright-field images of grains within the principal slip zone in calcite (a-c, VF 660) and olivine (d-f, SCO 1095). Grains contain dislocations (a, b, d, e) locally organised in dislocation walls (a, e). Grain boundaries are slightly curved suggesting non-equilibrium textures. Non-connected porosity is observed at triple junctions (b, c, f).

Supplementary Section IV | Raman spectroscopy

Due to the difficulty encountered in polishing and imaging anhydrite samples, Raman spectroscopy was used to characterise the nature of the material within the principal slip zone (PSZ) of sample AN 1031. Analysis was performed at the Department of Chemistry in Durham with the assistance of Prof A. Beeby. The analysis was conducted on the reflective mirror-like surface (MS), exposed in part of the sample used for microstructural imaging (AN 1031, Supplementary Figure 14). The MS splits the PSZ into two parts (Supplementary Figure 7). The spectrum reveals that the material is crystalline (sharp peaks) anhydrite (note the absence of water peaks between 3500 cm^{-1} and 1600 cm^{-1}).



Supplementary Figure 15 | Top view of the bottom cylinder (static) with the sheared sample ($v = 0.58\text{ ms}^{-1}$). Samples commonly split along mirror-like surfaces (in the case of AN 1031, within the PSZ, see Supplementary Figure 6).



Supplementary Figure 16 | Raman spectra⁷ of Gypsum ($\text{CaSO}_4 \cdot 2\text{H}_2\text{O}$), Bassanite ($\text{CaSO}_4 \cdot 0.5\text{H}_2\text{O}$) and Anhydrite (CaSO_4) compared with the spectra acquired on AN 1031 mirror-like surface (which exposes the material within the PSZ).

Supplementary Section V | Temperature calculation and thermal properties of rocks

During high-velocity rotary experiments it is not possible to directly measure the temperature with a thermocouple. A simple mono-dimensional equation for heat diffusion in a half space from a thin tabular source⁸ is utilised to estimate the temperature rise (ΔT) in the principal slip zone (PSZ). The non-adiabatic formulation is:

$$\Delta T(t) = \frac{1}{\rho c_P \sqrt{\pi \kappa}} \int_0^t \frac{\Phi(t')}{\sqrt{t-t'}} dt' \quad (1)$$

where ρ is the rock density, c_P is the specific heat, κ is the thermal diffusivity, Φ is the heat flux and t is time. This equation does not consider heat sinks (such as mineralogical reactions or phase changes) apart from heat diffusion from the shear zone.

The non-adiabatic formulation of Supplementary Equation 1 is valid only if the PSZ thickness is negligible compared to the length scale of heat diffusion, thus respecting:

$$W \ll 4\sqrt{(\kappa \delta / v)} \quad (2)$$

where W is the PSZ thickness, δ is the displacement and v is the slip rate (m/s).

If all the frictional work is converted into heat, the heat flow propagating on either side of the brittle shear band can be calculated by:

$$\Phi(t) = \frac{\tau(t)v(t)}{2} \quad (3)$$

where τ is the shear stress and σ_n is the normal stress. By substituting 3 into 1 we obtain:

$$\Delta T = \frac{1}{2\rho c_P \sqrt{\pi \kappa}} \int_0^t \frac{\tau(t')v(t')}{\sqrt{t-t'}} dt' \quad (4)$$

In the case of viscous flow in a narrow channel between two moving plates (PSZ), the temperature rise is expressed⁹ by:

$$\Delta T = \frac{1}{2\rho c_P W \sqrt{\pi \kappa}} \int_0^t \frac{\eta(t')v^2(t')}{\sqrt{t-t'}} dt' \quad (5)$$

where η is the viscosity of the material in the channel. The viscous shear stress is expressed by:

$$\tau_v(t) = \eta(t)\dot{\gamma}(t) \quad (6)$$

where $\dot{\gamma}(t) = v(t)W^{-1}$ is the shear rate. If W is small enough to satisfy Supplementary Equation 2 and assuming that the viscosity η is constant across the channel, thus :

$$\Delta T = \frac{1}{2\rho c_P \sqrt{\pi \kappa}} \int_0^t \frac{\eta(t')v(t')\dot{\gamma}(t')}{\sqrt{t-t'}} dt' = \frac{1}{2\rho c_P \sqrt{\pi \kappa}} \int_0^t \frac{\tau_v(t')v(t')}{\sqrt{t-t'}} dt' \quad (7)$$

τ_v corresponds to the measured bulk shear stress. Therefore Supplementary Equation 4 and Supplementary Equation 7 are equivalent and can be used to estimate the PSZ bulk temperature throughout the experiments.

It is assumed that the condition of Supplementary Equation 2 is met in all of the experiments as we observed PSZs thinner than 150 μm . It is important to note that the temperature rise calculated by Supplementary Equation 4 is an estimate, as no additional heat sinks are accounted for apart from heat diffusion. As reported in the main text, we did not observe the effect of endothermal processes such as thermal decomposition and melting (apart from the limited microstructural evidence of melting in the sodium chloride sample).

The thermal parameters used for the temperature calculations are reported in Supplementary Table 1.

Rock	ρ	Density kg m ⁻³	c_p	Thermal Capacity J Kg ⁻¹ K ⁻¹	κ	Thermal Diffusivity 10 ⁻⁶ m ² s ⁻¹
Anhydrite ¹⁰		2950		721		2.5
Calcite ¹¹		2700		700		1.48
Dolomite ¹⁰		2900		858		1.9
Sodium chloride ¹²		2160		916		1.2
Olivine (Fo91) ¹³⁻¹⁵		3340		1060		0.85

Supplementary Table 1 | Thermal properties (at 300 K) of rocks used in the experiments. References are reported below.

Supplementary Section VI | Normalized energies

From the best fit of experiments in this study it is possible to obtain A (Equation 1 in the main text), which is expected to correspond to the activation energy (Q) of the macroscopic ductile deformation normalized by the stress exponent (n) and the gas constant (R), $A = Q/nR$. Available values of Q/nR obtained from previous studies are reported here for comparison. Note that the referenced studies report values obtained at strain rates ($\dot{\gamma}, \dot{\epsilon}$) several orders of magnitude (> 6) lower than those in our high-velocity experiments.

Material	this work		previous work				References				
	$\dot{\gamma}$ (s ⁻¹)	D (μm)	$\dot{\epsilon}$ (s ⁻¹)		D (μm)	(n)		Q/nR (GSI)	(n)	Q/nR (GSS)	
Calcite	> 10 ³	< 0.8	1950.804		≤ 10 ⁻³	> 5	(4.7)	~ 7607	(1.7)	~ 15106	Schmid <i>et al.</i> , 1977 ¹⁶
Dolomite	> 10 ³	< 0.6	1238.735		≤ 10 ⁻⁴	≥ 2.5	(7)	~ 7216	(1.3)	~ 25906	Davis <i>et al.</i> , 2008 ¹⁷
Anhydrite	> 10 ³	< 0.3	648.712		≤ 10 ⁻³	≥ 10	(9.5)	~ 2785	(1)	~ 12028	Dell'Angelo and Olgaard, 1995 ¹⁸
Sodium Chloride	> 10 ³	< 8	815.215		≤ 10 ⁻⁵	> 100	(5.6)	~ 1718	-	-	Ter Heege <i>et al.</i> , 2005 (wet rocksalt) ¹⁹
Olivine (Fit 2)	> 10 ³	< 3	1472.210		< 10 ⁻⁴	≥ 2.7	(3)	~ 21288 ²⁰	(1.4)	~ 41579 ²¹	Karato and Jung, 2003 (averaged) ²⁰ Faul and Jackson, 2007 ²¹

Supplementary Table 2 | Normalized activation energies (A term in Equation 1 in the main text, where $A = Q/nR$) obtained from best fit of experimental data in this work and from previous literature. Where available, Q/nR values are reported along with the stress exponent (n) for grain size-insensitive (GSI) and grain size-sensitive (GSS) creep. Most experiments were performed in fine-grained aggregates (grain sizes $D < 10 \mu\text{m}$) at variable conditions (high-temperature and high-pressure conditions) and much lower strain rates. Note that the referenced experiments are compression tests, hence, strain rates are indicated with $\dot{\epsilon}$ rather than $\dot{\gamma}$ (shear strain rate). References are reported below.

It is worth noting that best fit parameters reported in literature are observed to evolve with incremental deformation^{22,23}, and can be considered constant only for limited ranges of strain²². Only a few studies report shear strains larger than 10 before failure^{22,24}, whereas rock deformation at extreme, seismic shear strains ($>> 10^3$) and strain rates $> (10^3 \text{ s}^{-1})$ has not been previously explored. A direct comparison between flow law parameters here derived and those measured at low strain and strain rates could thus be potentially misleading. Future research should systematically investigate whether these differences are due to a change in interplay between the specific operating mechanisms, or to the intrinsic semi-empirical nature of the best fit parameters in the flow laws²⁵.

Supplementary information references

1. Pozzi, G., De Paola, N., Nielsen, S. B., Holdsworth, R. E. & Bowen, L. A new interpretation for the nature and significance of mirror-like surfaces in experimental carbonate-hosted seismic faults. *Geology* 46, 583–586 (2018).
2. Covey-Crump, S. J. The normal grain growth behaviour of nominally pure calcitic aggregates. *Contrib. to Mineral. Petrol.* 129, 239–254 (1997).
3. De Paola, N., Holdsworth, R. E., Viti, C., Collettini, C. & Bullock, R. Can grain size sensitive flow lubricate faults during the initial stages of earthquake propagation? *Earth Planet. Sci. Lett.* 431, 48–58 (2015).
4. Thieme, M., Demouchy, S., Mainprice, D., Barou, F. & Cordier, P. Stress evolution and associated microstructure during transient creep of olivine at 1000–1200 °C. *Phys. Earth Planet. Inter.* 278, 34–46 (2018)
5. Hielscher, R. & Schaebein, H. A novel pole figure inversion method: Specification of the MTEX algorithm. *J. Appl. Crystallogr.* 41, 1024–1037 (2008).
6. Bachmann, F., Hielscher, R. & Schaebein, H. Texture Analysis with MTEX – Free and Open Source Software Toolbox. *Solid State Phenom.* 160, 63–68 (2010).
7. Liu, Y. et al. Raman, MIR, and NIR Spectroscopic Study of Calcium Sulfates: Gypsum, Bassanite, and Anhydrite. *LPI* 2128 (2009).
8. Rice, J. R. Heating and weakening of faults during earthquake slip. *J. Geophys. Res. Solid Earth* 111, B05311 (2006).
9. Turcotte, D. L. & Schubert, G. Geodynamics 3rd edition. *Cambridge University Press.* (2014).
10. Di Toro, G. et al. Fault lubrication during earthquakes. *Nature* 471, 494–499 (2011).
11. De Paola, N., Holdsworth, R. E., Viti, C., Collettini, C. & Bullock, R. Can grain size sensitive flow lubricate faults during the initial stages of earthquake propagation? *Earth Planet. Sci. Lett.* 431, 48–58 (2015).
12. Smith, D. D. Thermal conductivity of halite using a pulsed laser. (1976). doi:10.2172/7228316
13. Xu, Y., Shankland, T. J., Linhardt, S., Rubie, D. C., Langenhorst, F. and Klasinski, K. (2004) ‘Thermal diffusivity and conductivity of olivine, wadsleyite and ringwoodite to 20 GPa and 1373 K’, *Physics of the Earth and Planetary Interiors*. Elsevier, 143–144, pp. 321–336. doi: 10.1016/J.PEPI.2004.03.005.
14. Clauser, C. and Huenges, E. (2013) ‘Thermal Conductivity of Rocks and Minerals’, in. *American Geophysical Union (AGU)*, pp. 105–126. doi: 10.1029/RF003p0105.
15. Su, C., Liu, Y., Song, W., Fan, D., Wang, Z. and Tang, H. (2018) ‘Thermodynamic properties of San Carlos olivine at high temperature and high pressure’, *Acta Geochimica. Science Press*, 37(2), pp. 171–179. doi: 10.1007/s11631-018-0261-z.
16. Schmid, S. M., Boland, J. N. and Paterson, M. S. Superplastic flow in finegrained limestone, *Tectonophysics*, 43(3–4), pp. 257–291. doi: 10.1016/0040-1951(77)90120-2 (1977).
17. Davis, N. E., Kronenberg, A. K. and Newman, J. Plasticity and diffusion creep of dolomite, *Tectonophysics*. Elsevier, 456(3–4), pp. 127–146. doi: 10.1016/J.TECTO.2008.02.002 (2008).
18. Dell’Angelo, L. N. and Olgaard, D. L. Experimental deformation of fine-grained anhydrite: Evidence for dislocation and diffusion creep, *Journal of Geophysical Research: Solid Earth*, 100(B8), pp. 15425–15440. doi: 10.1029/95jb00956 (1995).
19. Ter Heege, J. H., De Bresser, J. H. P. and Spiers, C. J. Rheological behaviour of synthetic rocksalt: the interplay between water, dynamic recrystallization and deformation mechanisms, *Journal of Structural Geology*. Pergamon, 27(6), pp. 948–963. doi: 10.1016/J.JSG.2005.04.008 (2005).
20. Karato, S. I. and Jung, H. Effects of pressure on high-temperature dislocation creep in olivine, *Philosophical Magazine*, 83(3), pp. 401–414. doi: 10.1080/0141861021000025829 (2003).
21. Faul, U. H. and Jackson, I. Diffusion creep of dry, melt-free olivine, *Journal of Geophysical Research: Solid Earth*. John Wiley & Sons, Ltd, 112(4). doi: 10.1029/2006JB004586 (2007).
22. Mackwell, S. J. & Paterson, M. S. New developments in deformation studies: High-strain deformation.

Reviews in Mineralogy and Geochemistry 51, 1–19 (2002).

23. Pieri, M., Burlini, L., Kunze, K., Stretton, I. & Olgaard, D. L. Rheological and microstructural evolution of Carrara marble with high shear strain: Results from high temperature torsion experiments. *J. Struct. Geol.* 23, 1393–1413 (2001).
24. Barnhoorn, A., Bystricky, M., Burlini, L. & Kunze, K. The role of recrystallisation on the deformation behaviour of calcite rocks: Large strain torsion experiments on Carrara marble. *J. Struct. Geol.* 26, 885–903 (2004).
25. Frost, H. J. & Ashby, M. F. Deformation-mechanism maps: the plasticity and creep of metals and ceramics. *Pergamon Press* (1982).